

This is the author's final, peer-reviewed manuscript as accepted for publication (AAM). The version presented here may differ from the published version, or version of record, available through the publisher's website. This version does not track changes, errata, or withdrawals on the publisher's site.

Considerations for the Use of *STEREO*-HI Data for Astronomical Studies

S. J. Tappin

Published version information

Citation: Tappin, SJ. "Considerations for the use of STEREO-HI data for astronomical studies." *The Astronomical Journal*, vol. 153, no. 4 (2017): 164.

doi: [10.3847/1538-3881/aa6349](https://doi.org/10.3847/1538-3881/aa6349)

This version is made available in accordance with publisher policies. Please cite only the published version using the reference above.

This item was retrieved from **ePubs**, the Open Access archive of the Science and Technology Facilities Council, UK. Please contact epubs@stfc.ac.uk or go to <http://epubs.stfc.ac.uk/> for further information and policies.

CONSIDERATIONS FOR THE USE OF STEREO HI DATA FOR ASTRONOMICAL STUDIES

S. J. TAPPIN¹

¹*RAL Space, STFC Rutherford Appleton Laboratory, Harwell Oxford, Didcot, Oxon. OX11 0QX, UK.*

ABSTRACT

Recent refinements to the photometric calibrations of the Heliospheric Imagers (HI) onboard the Solar TERrestrial RElations Observatory (STEREO) (Tappin, Eyles, & Davies 2015, 2017) have revealed a number of subtle effects in the measurement of stellar signals with those instruments. These effects need to be considered the interpretation of STEREO-HI data for astronomy. In this paper we present an analysis of these effects and how to compensate for them when using STEREO-HI data for astronomical studies. We determine how saturation of the HI CCD detectors affects the apparent count rates of stars after the onboard summing of pixels and exposures. Single-exposure calibration images are analyzed and compared with binned and summed science images to determine the influence of saturation on the science images. We also analyze how the onboard cosmic-ray scrubbing algorithm affects stellar images. We determine how this interacts with the variations of instrument pointing to affect measurements of stars. We find that saturation is a significant effect only for the brightest stars, and that its onset is gradual. We also find that degraded pointing stability, whether of the entire spacecraft or of the imagers leads to reduced stellar count rates and also increased variation thereof through interaction with the onboard cosmic ray scrubbing algorithm. We suggest ways in which these effects can be mitigated for astronomical studies and also suggest how the situation can be improved for future imagers.

Keywords: Instrumentation: miscellaneous – Space vehicles: instruments – Techniques: photometric

CONSIDERATIONS FOR THE USE OF STEREO HI DATA FOR ASTRONOMICAL STUDIES

S. J. TAPPIN¹

¹*RAL Space, STFC Rutherford Appleton Laboratory, Harwell Oxford, Didcot, Oxon. OX11 0QX, UK.*

Keywords: Instrumentation: miscellaneous – Space vehicles: instruments – Techniques: photometric

1. INTRODUCTION

The Solar Terrestrial Relations Observatory (STEREO: Kaiser et al. (2008)), launched in late 2006, is a two-spacecraft NASA mission to investigate the initiation and propagation of coronal mass ejections (CMEs) from locations separated in ecliptic longitude. The two spacecraft were placed in heliocentric orbits, one (the ahead spacecraft; STEREO-A) somewhat inside 1 AU and the other (the behind spacecraft; STEREO-B) somewhat outside. This means the spacecraft drift ahead of and behind the Earth by about 22° per year, and both spacecraft reached solar superior conjunction in early 2015. Science operations from the STEREO spacecraft began on 1 Apr. 2007. STEREO-A is still operating, but unfortunately contact with STEREO-B was lost on 1 Oct. 2014 during preparations for solar conjunction. Recently (Aug.-Sep. 2016) signals from STEREO-B were detected, but as of the time of writing attitude control has not been restored.

The imaging capabilities of STEREO are provided by the Sun Earth Connection Coronal and Heliospheric Investigation (SECCHI: Howard et al. (2008)), which is a package consisting of an extreme ultra-violet imager (EUVI), two coronagraphs (COR1 and COR2), and two Heliospheric Imagers (HI-1 and HI-2: Eyles et al. (2009)). EUVI and the CORs are collectively referred to as the Sun Centered Instrument Package (SCIP). The HIs use Thomson-scattered light to detect and track CMEs and other solar-wind disturbances from the outer limits of the coronagraph fields of view to 1 AU and beyond. The HI cameras have a nominally circular field of view offset from the Sun to the earthward side (after solar conjunction STEREO-A was rolled by 180° to maintain this alignment). The inner (HI-1) cameras have a field of view 20° in diameter, centered at an elongation of 14° . While the outer (HI-2) cameras have a field diameter of 70° centered at an elongation of 53° . In practice, for HI-1 the whole square field of view is usable, but for HI-2 little useful data can be recovered from outside the nominal circular field.

The HIs observe a relatively large area of sky with a cadence of 40 minutes for the HI-1 instruments and two hours for HI-2. Over the course of a solar orbit, each camera scans a swath of sky centered on the ecliptic, for the HI-1 cameras this covers ecliptic latitudes $\pm 10^\circ$ (or about 17% of the sky) and for HI-2 the range is $\pm 35^\circ$ (about 57% of the sky), this coverage is illustrated in Fig. 1. Apparitions of a particular star recur each orbit, which is about 345 days for STEREO-A and 389 days for STEREO-B. At any apparition a star which is close to the ecliptic plane remains in the field of view for about 20 days for HI-1 and 50-60 days for HI-2, and for

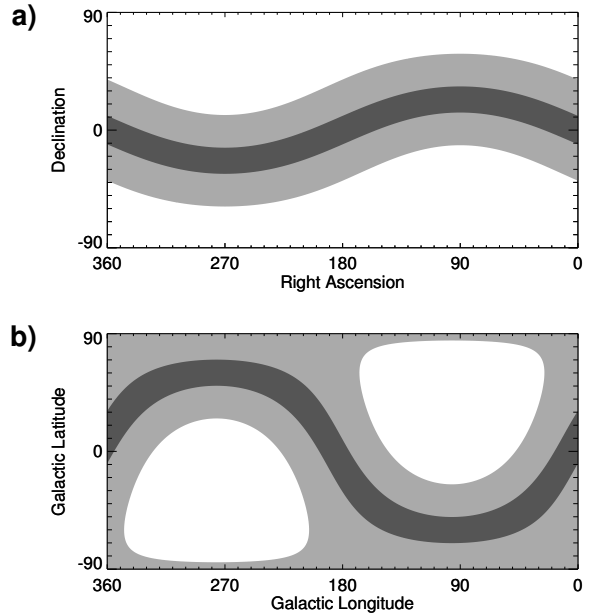


Figure 1. Coverage of the sky by the HI cameras. a) In RA and Dec, b) In galactic coordinates. Dark gray shows HI-1 coverage, Light Gray shows HI-2 coverage.

a shorter period for stars near the latitude limits of the field of view. For HI-1 the functional magnitude limit is about 10, while for HI-2A it is about 8 and for HI-2B (which is significantly defocussed; (Eyles et al. 2009)) the limit is about 7. This wide-field monitoring means that the observations have great value for astronomical work, particularly for investigations requiring the long-term monitoring of large numbers of bright stars. The HIs observe close to the ecliptic plane, an area generally avoided by dedicated astronomical monitoring instruments (Sangaralingam & Stevens 2011), and so provide coverage hard to obtain elsewhere.

Examples of published astronomical studies using data from the HI cameras include: exoplanet searches (e.g. Sangaralingam & Stevens 2011; Wraight et al. 2011; Whittaker, Stevens, & Sangaralingam 2013); eclipsing binaries (e.g. Wraight et al. 2012c; Chaturvedi et al. 2014; Belcheva et al. 2015); cataclysmic variables (e.g. Holdsworth et al. 2014); as well as longer timescale intrinsic variability (e.g. Wraight et al. 2012a,b; Paunzen et al. 2013). Valtonen et al. (2011) even discuss the possibility of using HI data in an investigation of black-hole physics. However, the HIs were designed for the study of diffuse coronal and heliospheric structures, and not for stellar observations. Also, as with any instrument, there are limitations that are encountered when the instrument is pushed close to its capabilities. In particular, during the calibration analyses for the HIs which used stellar measurements, Tappin, Eyles, & Davies (2015)

and Tappin, Eyles, & Davies (2017) found a number of effects which could, if not properly accounted for, cause erroneous conclusions to be drawn when using HI data for astronomical studies. This was counterbalanced by the realization that relative photometry can with care be taken to more than an order of magnitude greater precision than absolute photometry (i.e. the main error sources are systematic effects that remain constant for any given star). In this study we therefore concentrate on effects that may limit the precision of such relative photometry. It has also been shown by Tappin, Eyles, & Davies (2015) and Tappin, Eyles, & Davies (2017) that all of the HI camera systems have exceptionally good long-term stability with a degradation rate slower than 0.2% per year.

In Sect. 2 we summarize the main processing that is carried out onboard the spacecraft, and also the stages in the generation of HI images. In Sect. 3 we consider how saturation effects interact with the onboard summing of exposures and pixels. In Sect. 4 we look at how bright features are affected by the interaction of cosmic ray scrubbing algorithm with fluctuations in the camera pointing, and with the orbital motion of the spacecraft.

2. HI IMAGING

Unlike the images from the SECCHI coronagraphs (COR1 and COR2: Howard et al. (2008)), the HI science images are not single exposures of an effectively static sky. To detect sufficient photons to track structures propagating through the solar wind, the HIs need integration times of many minutes. However if this were done as a single exposure, the number of particle hits on the detectors would make the resulting images unusable. Therefore the images are created by taking many shorter exposures, removing particle hits and summing onboard (Eyles et al. 2009).

Nominally, 36 science images from each of the HI-1 cameras, and 12 from each of the HI-2 cameras are generated each day. For just over a year around solar conjunction the small angular separation of the spacecraft and the Sun (as seen from Earth) meant that the telemetry rate was severely limited and so images were returned at reduced cadence and resolution. For STEREO-A this interval was from 17 Aug. 2014 to 16 Nov. 2015. The images from this interval are of low resolution and used a lossy compression algorithm they are therefore unlikely to be of use for astronomy, so we will not consider them further in this paper.

In addition to the science images, one single-exposure full-resolution image is transmitted to Earth from each imager on most days for performance monitoring. The only onboard processing applied to these calibration im-

ages is the subtraction of the DC bias. In this paper we make use of these images to shed light on the effects of the onboard processing on the science images.

2.1. Cosmic ray removal

After the exposures have been read out from the CCD the bias is subtracted. The bias is a DC offset applied to ensure that the readout voltage is always positive.

The next stage of the onboard processing is the scrubbing of energetic particle hits. The algorithm used looks for large increases in counts between successive exposures and replaces those high counts with the value from the previous exposure (Eyles et al. 2009). For all images taken during normal science operations (i.e. since April 2007), the least aggressive setting of this method has been used. In this configuration, any pixel value which exceeds the corresponding pixel value in the previous exposure by more than 5σ is replaced by the pixel value from the previous exposure, i.e. if we denote the counts in the current exposure by I_c and the counts in the previous exposure by I_p then the scrubbed exposure I'_c is given by:

$$I'_c = \begin{cases} I_p; & \text{Where } (I_c - I_p) \sqrt{\frac{15}{I_c}} > 5 \\ I_c; & \text{Elsewhere} \end{cases}, \quad (1)$$

(Eyles et al. (2009); D. Wang, private communication 2015), where the factor of $\sqrt{15}$ comes from the fact that 1 digitizer number (DN) corresponds to 15 photoelectrons. While the locations of cosmic ray edits are not recorded, the total number removed from each exposure is recorded in the final bytes of the image readout data stream. These values are preserved in the Level-0 images but are removed in the processing to generate the Level-1 and 2 images. Note that in HI-B images before conjunction and HI-A images afterwards the rotation of the image to bring North to the top means that the values are at the start of the image.

2.2. Binning and summing

It is not possible to transmit all of the exposures back to Earth. Therefore they are first binned from 2048×2048 pixels to 1024×1024 bins. The binned exposures are then summed to give an integrated image which is returned (Eyles et al. 2009). For HI-1, the normal science images are a sum of 30 40-second exposures taken at a one minute cadence, one such image is generated every 40 minutes with a total integration time of 20 minutes. For HI-2, the science images are a sum of 99 50-second exposures also with a one-minute cadence giving an integration of 82.5 minutes, these are taken every two hours.

In addition to allowing the removal of particle hits, the summing and binning increases the effective dynamic range from the 14 bits of the raw exposures to about 21 bits for HI-1 and between 22 and 23 bits for HI-2, albeit with an increased noise level as the readout noise is present in each exposure.

2.3. Post processing

After the images are received by the ground stations, further processing is required to create a usable data product. The processing pipeline is described by Eyles et al. (2009), and on the UK Solar System Data Centre (UKSSDC) web site (http://www.ukssdc.ac.uk/solar/stereo/documentation/HI_processing.html and http://www.ukssdc.ac.uk/solar/stereo/documentation/HI_processing_L2_data.html). In summary:

- The raw images are converted from units of DN to units of $\text{DN s}^{-1} (\text{CCD pixel})^{-1}$. At this stage the integer values are also converted to floating point values.
- The readout smearing caused by the shutterless operation of the cameras (Eyles et al. 2009) is corrected.
- Columns containing severely saturated bins (those with an average of more than 14,000 DN per pixel per exposure) are set to the IEEE Not-a-number (NaN) value. It is necessary to flag the entire column as the de-smearing does not work correctly when there are saturated pixels in the column.
- The large-scale flatfield correction determined by Bewsher et al. (2010) (HI-1) or by Tappin, Eyles, & Davies (2015) (HI-2) is applied.
- The pointing information in the header is corrected by matching star locations in the image with catalog positions in the manner described by Brown, Bewsher, & Eyles (2009).
- Additional images are also produced in units of B_{\odot} , and S10, by applying the appropriate conversion factors as determined by Bewsher et al. (2010), Tappin, Eyles, & Davies (2015) and Tappin, Eyles, & Davies (2017). Corrections for the effect of projected pixel size on the surface brightness of extended structures are applied to these images (Tappin, Eyles, & Davies 2015). N.B. because of this extended-source correction it is generally more appropriate to use the images in $\text{DN s}^{-1} (\text{CCD pixel})^{-1}$ for astronomical studies.

The resulting images are referred to as Level-1 images.

Level-2 images have an extra step in which the F-corona (and any other slowly-varying background) is removed by subtracting a one (three for HI-2) or eleven-day running mean of the lowest quartile of the measurements for each bin.

The single-exposure full-resolution images are processed to Level-1, but are not included in the Level-2 processing.

All HI images at each processing level can be downloaded from the UKSSDC (<http://www.ukssdc.ac.uk/solar/stereo/data.html>). The routines for generating the Level-1 and 2 images are available as part of the STEREO/SECCHI package in the SolarSoft system (Freeland & Handy 1998).

3. SATURATION EFFECTS

Since the exposure times of the HIs are optimized for observing the solar wind, the brightest stars in the field saturate the CCD detectors. However as a result of the on-board binning and summing the onset of saturation in the science images is a “soft” event as a star may not saturate all of the pixels in a bin and not all of the exposures within an image. In addition, for reasons which are discussed below, the onset of saturation depends on the location of the star in the field of view. Therefore, it may not be obvious without careful analysis whether a particular stellar image is affected by saturation. In this section we attempt to estimate the stellar magnitudes at which the effects of saturation must be considered.

Since the HI analogue-to-digital (A-to-D) converters reach saturation slightly below the full-well level of the CCD, the onset of saturation can be characterized as when the brightest pixel of the object of interest reaches the maximum possible value of $2^{14} - \text{bias} - 1$ in any exposure of the image. The value of bias varies from imager to imager but is in the region of 700 DN and has remained constant to better than 1 DN over the mission for each imager.

To determine the effects of saturation on stars in the HI science images we begin with an analysis of the single-exposure full-resolution calibration images, of which one is transmitted from each instrument on most days. In these images, where there is neither binning nor summing of pixels, saturation can be readily identified in the Level-0 data. In Fig. 2 we show the 90th percentile counts in the highest pixel of each of the brighter stars in the calibration samples as described by Tappin, Eyles, & Davies (2015, 2017) (including those stars that were too bright to be used in the calibration analysis) plotted as a function of the photonic magnitude of the star (Tappin, Eyles, & Davies 2015). All of the single-exposure images

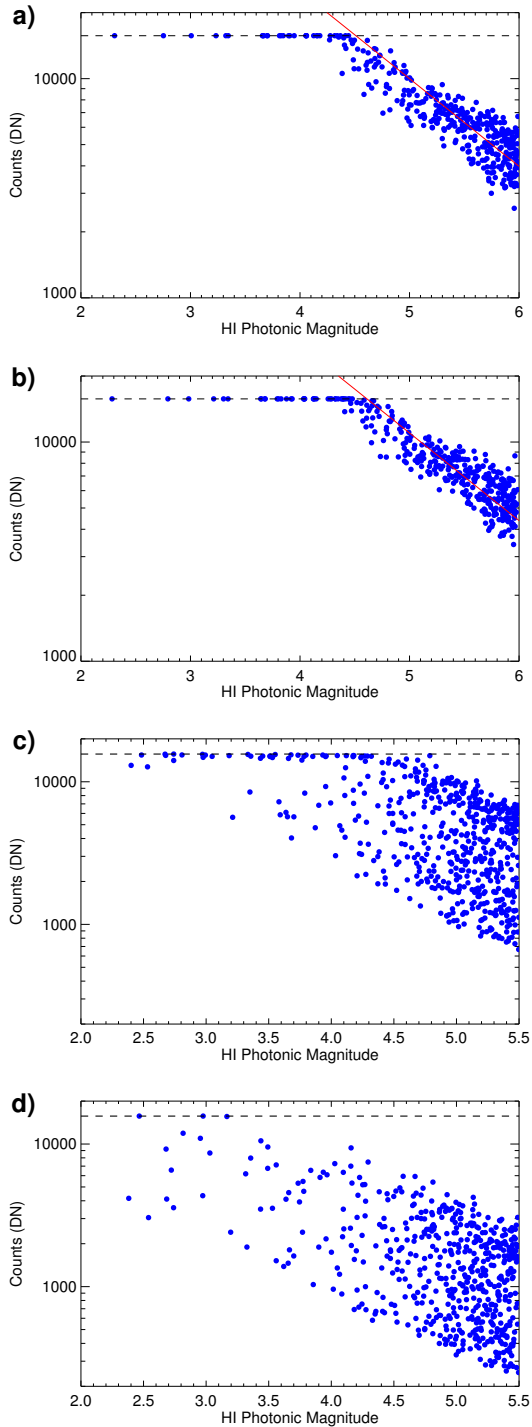


Figure 2. 90th percentile values of the counts in the brightest pixel for each of the brighter calibration stars in the Level-0 calibration images as a function of photonic magnitude. a) HI-1A, b) HI-1B, c) HI-2A, and d) HI-2B. The horizontal dashed line in each panel shows the maximum possible counts. The red line in the HI-1 panels shows the expected slope of the trend, the level is not significant.

taken between April 2007 and October 2014 were used. A star that lies on the saturation limit in these plots has at least one saturated pixel in at least one exposure in ten. The behavior for the two HI-1 instruments is close to what one would naively expect, with the counts increasing with decreasing magnitude until they reach the saturation limit near to magnitude 4.5. However a closer inspection shows that for the faintest stars shown here, there are slightly more counts than would be expected from the theoretical slope (indicated by the red lines in Fig. 2a and b, note that these only indicate the slope, the level is only estimated). For HI-2 the general trend is similar, but there is a very large scatter of the counts for any magnitude. We also note that for HI-2B there are very few stars that reach the saturation level.

The deviation of the fainter stars above the expected counts in HI-1 is found to be greatest at small elongations. This is caused by the fact that at the sunward edge of the field of view, the F-coronal background is about 60% of the saturation level (Eyles et al. 2009), while at the anti-sunward edge it is only about 1%. The peak pixel count is the sum of the peak counts from the star and the counts from the F-corona. Therefore even stars that are bright compared with the F-corona near the outer parts of the field of view will have a major coronal contribution near to the inner edge, and since the F-coronal contribution does not depend on the stellar brightness the effect is proportionally larger for fainter stars.

In HI-2 the maximum F-coronal signal is only about 10% of the saturation level, so any effect due to the F-corona is lost in the large scatter of the counts. Rather, the peak count of a star falls off with radial distance from the center of the field of view. This is entirely consistent with the fact that the point spread function (PSF) in HI-2 becomes broader in the outer parts of the field of view, and in addition in the outermost regions of the field there is significant vignetting (Tappin, Eyles, & Davies 2015). The lower peak counts in HI-2B compared with HI-2A are explained by the defocussing of the HI-2B optics (Eyles et al. 2009), which results in a much larger PSF in HI-2B than in HI-2A.

To get a better picture of the onset of saturation, we therefore need to divide the field of view into a number of regions in which the stars show broadly similar behavior. Since for HI-1 the dominant effect is the level of the F-corona (i.e. the solar elongation angle), we have found that an effective subdivision is to split the image region into rectangles (we have used five boxes in the CCD-x direction and three in the y direction, Fig. 3a). For HI-2, where the dominant factors are the variation of the PSF and of the large-scale flat field, it is more ap-

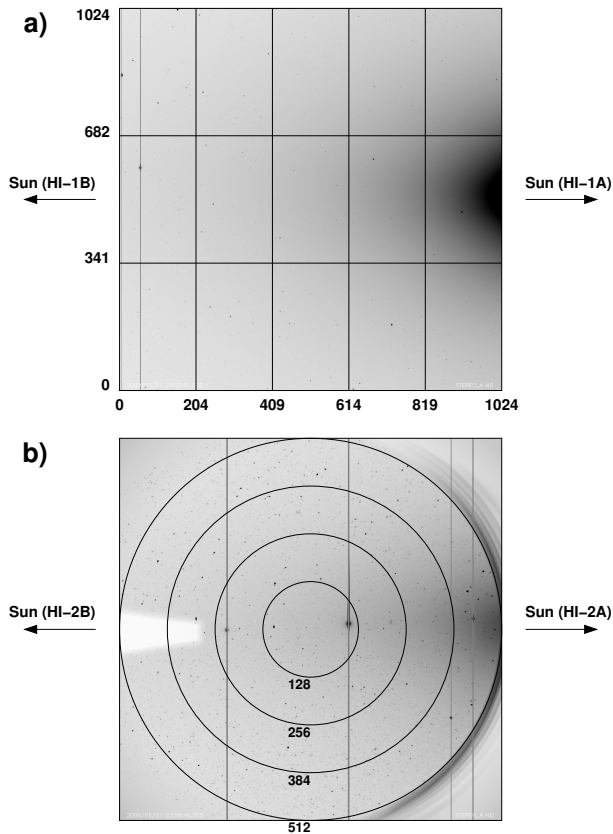


Figure 3. The sub-regions used for the saturation analysis. a) HI-1, b) HI-2. The coordinates are the lower bounds of each region, given in science image bins. The region beyond the outer circle in b) is outside the nominal field of view and has not been analyzed. The background images are Level-1 HI-A images from 1 May 2009, square root scaled from 0 to 200 $\text{DN s}^{-1} (\text{CCD pixel})^{-1}$ for HI-1, and 0 to 100 $\text{DN s}^{-1} (\text{CCD pixel})^{-1}$ for HI-2. The vertical streaks in the HI-2 image in b) are columns flagged as being saturated.

appropriate to divide the field into concentric annuli (here we use four annuli, or to be pedantic a disc and three annuli, Fig. 3b). In Fig. 4 we show the relation between magnitude and maximum counts for a selection of these regions of the CCD in a similar format to Fig. 2.

For the HI-1 measurements (Fig. 4a and b), we can see that the effects of CCD position are most evident for the fainter stars where those at smaller elongations have higher maximum counts (and a wider spread) as expected from the contribution of the F-corona. Since the Level-0 images do not have any background subtraction or flat-field corrections applied, this is nothing more than the addition of the F-corona signal to the stellar signal. This addition of the signals means that stars saturate more readily at small elongations. The onset of saturation lies at about magnitude 4.5 at the edge furthest from the Sun, and about 4.8 close to the Sun, with little difference between HI-1A and HI-1B.

For HI-2 (Fig. 4c and d), the differences are much more dramatic, with a factor of at least five between the peak counts near the field center and those near the edge. There is also a marked difference, of approximately a factor of three, between HI-2A and HI-2B. Here, the changes are driven by the variation of the PSF across the field-of-view, and also the fall-off of sensitivity in the outer field (Tappin, Eyles, & Davies 2015). For HI-2A, near the center of the field of view stars begin to be saturated at a magnitude of about 4.8 (similar to HI-1) but near the edge saturation does not occur until about magnitude 3.0. For HI-2B, near the center of the field of view, saturation starts at about magnitude 3.3 but we do not see any saturation at all near the edge.

In normal circumstances, scientific analysis of stellar signals will be carried out not with the maxima of the calibration images, but rather with integrated counting rates from the science images. There are two implications of this. Firstly, any saturated pixels will be added to unsaturated values (both by the onboard summing and also by the integration across the PSF), meaning that the hard cutoff will not occur. Secondly, the application of the flat-field correction and the subtraction of backgrounds (whether by the photometry routines or by the background models used in Level-2 images) will tend to neutralize the variations across the CCD that were evident in Fig. 4. In Figs. 5 and 6 we show the comparisons of the maxima and integrated rates, from both the calibration and science images, for HI-1 and for HI-2 respectively. The line on the plots is an L1-norm (least absolute residual) fit to the fainter stars (magnitude > 5.0 for HI-1, > 4.5 for HI-2) of the expected variation of the parameter with magnitude, i.e.:

$$y = A \cdot 10^{-0.4m}, \quad (2)$$

where y is the maximum counts or integrated count rate, m is the photonic magnitude and A is the fitted scaling parameter.

Figures 5b, e and 6b, e show how in science images the saturation onset for the peak bin is a gradual process as, apart from the very brightest stars, the brightest bin is likely to be a sum of saturated and unsaturated pixels. Summing over the PSF to generate integrated rates (Figs. 5c, and f and 6c and f) further slows the onset of saturation as more unsaturated bins are included in the sum, and there is no longer a visible cutoff as even the brightest stars are not saturated over the entire PSF. However, there is still a significant deviation from the fitted trend for the brightest stars. On logarithmic plots such as Figs. 5 and 6 the effects on the rates may appear insignificant, but are in fact of the order of 20% for the brightest stars (brighter than magnitude 3) near the

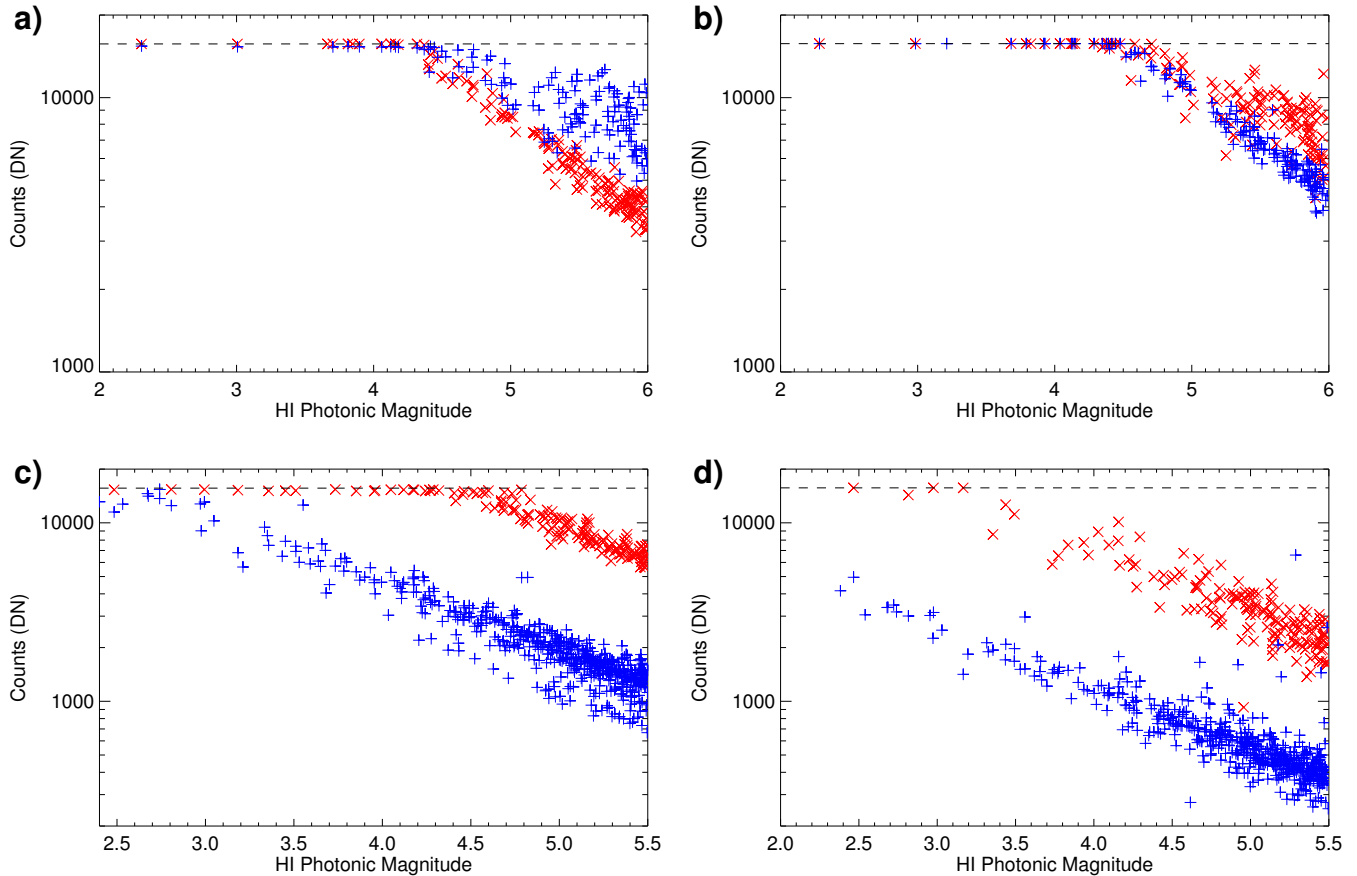


Figure 4. Demonstration of the effect of the position of the stellar image on the CCD on the measured maximum counts. The format is the same as for Fig. 2. a) HI-1A, b) HI-1B, c) HI-2A, and d) HI-2B. For the HI-1 panels, the red \times symbols show the values for the box with CCD- x range 0 to 203 (bins) and y range 341 to 681, while the blue $+$ symbols show the values for the box with x range 819 to 1023 and the same y range. For the HI-2 panels the red \times symbols show the values in the disc out to 127 bins, and the blue $+$ symbols show the values in the annulus from 384 to 511 bins. In each case the values plotted are the 90th percentile of the maximum pixel of the star while it is in the CCD region defined.

center of the HI-2A field of view, and close to a factor of 2 for the brightest stars in HI-1. It should also be noted here that the combination of the flat field corrections applied to the Level-1 images and the integration and background removal of the photometry removes the large scatter seen in the plots of maximum pixels or bins.

4. POINTING EFFECTS

As described above in Sect. 2, the first stage of the on-board image processing is the scrubbing of cosmic ray hits. Since this algorithm works simply by comparing the value of a pixel with its value in the previous exposure, this procedure has no context and thus a real rapid change in signal, such as might be expected when a bright star moves significantly between exposures, may be flagged as a particle hit and “corrected”. We have found three circumstances in which this occurs:

- For all instruments, after the switch to gyroless pointing control, when the roll stability of the spacecraft was reduced.
- For HI-1B only, when its pointing relative to the spacecraft pointing shifts.
- For all instruments, at all times through the motion of bright stars across the field of view.

We will consider these in turn.

4.1. Gyroless attitude control

During the analysis of the evolution of the HI-1 responses Tappin, Eyles, & Davies (2017) found that there was an abrupt drop in the apparent gains late in the observation series. They determined that this occurred at the times of the change to gyroless attitude control. A similar drop was also present in the HI-2 data.

For most of the STEREO mission prior to superior conjunction, the attitude control loop of the

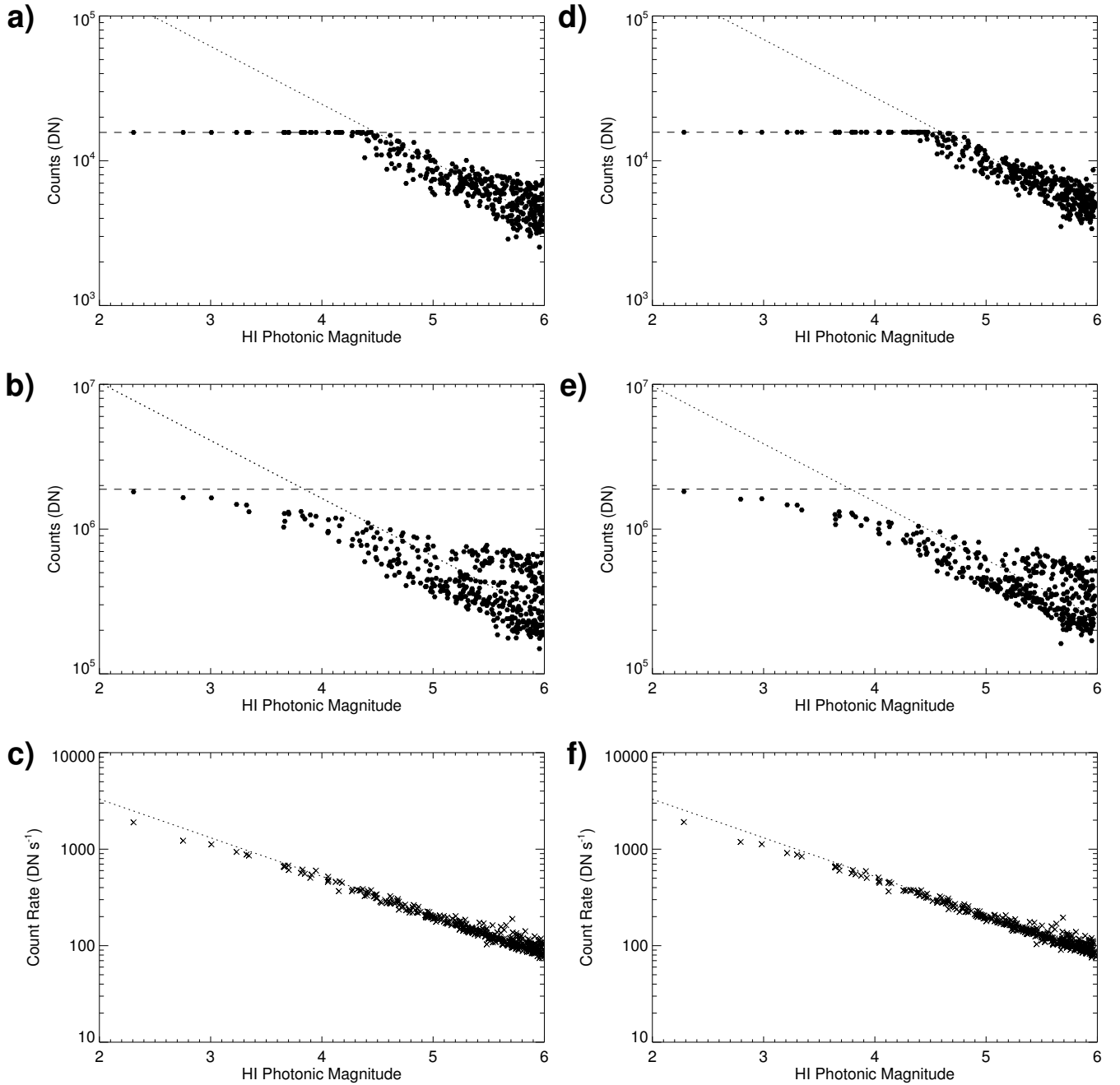


Figure 5. Comparison of the saturation onsets in single exposure and science images for both maxima and integrated rates (using a 3 bin/6 pixel photometry aperture) for HI-1. a-c) HI-1A, d-f) HI-1B. a,d) The 90th percentile of the maximum values for each star in the Level-0, full-resolution calibration images. b,e) The 90th percentile of the maxima in the Level-0 binned science images. And c,f) The median integrated count rates from the Level-1 science images. The dotted lines show the best fit of the form $y = A \cdot 10^{-0.4m}$ to stars fainter than magnitude 5.0. The horizontal dashed line in the plots of maxima shows the theoretical saturation level.

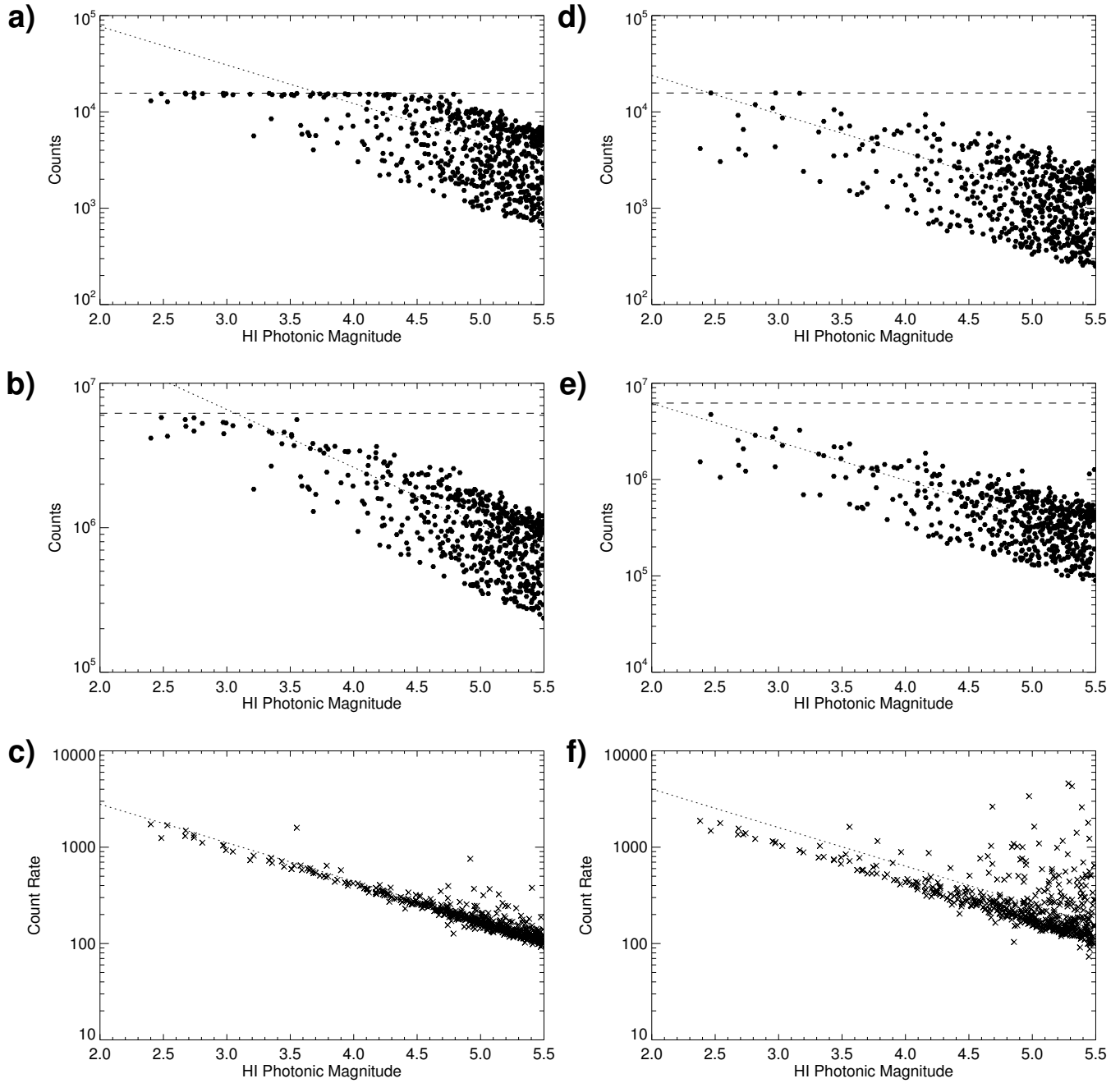


Figure 6. Comparison of saturation onsets in single exposure and science images for both maxima and integrated rates (using the “descents” photometry method of [Tappin, Eyles, & Davies \(2015\)](#)) for HI-2. a-c) HI-2A. d-e) HI-2B. The format is identical to Fig. 5, except that the fits are done for stars fainter than magnitude 4.5.

two spacecraft was closed using pointing information from onboard gyros. However during 2013, it became apparent that the gyro systems were nearing their end of life. This issue was particularly pressing for STEREO-A, which was already operating on its backup system as the primary system had failed soon after launch (for discussions of the problem see <http://stereo-ssc.nascom.nasa.gov/minutes/>, and in particular http://stereo-ssc.nascom.nasa.gov/minutes/2013/weekly_20130723.txt). As a result of this, a decision was taken to turn off the attitude sensing gyros during normal operations and close the attitude control loop solely with the guide telescope and star trackers. This change was implemented on 18 Sep. 2013 for STEREO-A and 7 Jan. 2014 for STEREO-B. The change resulted in significantly degraded stability about the spacecraft roll axis, although it was still well within the original pointing requirements as described in [Driesman, Hynes, & Cancro \(2008\)](#). The attitude control tolerance specifications for STEREO were driven by the requirements of the SCIP instruments rather than the HIs. Because of this, the pointing requirements specify only tolerances for absolute pointing, and for jitter on the timescales of the polarization sequences of the coronagraphs. In addition the requirements for roll are much less stringent than those for yaw and pitch.

[Tappin, Eyles, & Davies \(2017\)](#) showed that the drop in gain was caused by the cosmic ray scrubbing of stellar pixels due to the reduced pointing stability in gyroless operation. In that study, the authors merely noted the issue and chose not to use data collected after the gyros were turned off. Here we attempt to quantify the apparent gain reduction and also the increase in the variance of the count-rate measurements for all four instruments caused by this change.

To examine the effects of the reduced pointing stability on the HI data, we need a measure of that stability on the timescales of the HI exposure cadence, i.e. 1 minute. For this we take the spacecraft attitude information (from GET_STEREO_ROLL, in the STEREO package of SolarSoft) at a 1 second cadence, and form 1 minute averages. We then define the 1 minute fluctuation (F_1) over an N -minute interval as:

$$F_1 = \sqrt{\frac{\sum_{i=1}^{N-1} (P_{i+1} - P_i)^2}{N-1}}, \quad (3)$$

where P_i is the i th pointing value and N is the total number of values, i.e. the rms difference between successive 1-minute averages. This can be computed separately for each of the components; roll, pitch and yaw, and we can also combine them to obtain a net fluctuation at a given

elongation (ϵ) as:

$$F_1(\epsilon) = \sqrt{F_1(\text{yaw})^2 + (F_1(\text{roll}) \sin \epsilon)^2 + (F_1(\text{pitch}) \cos \epsilon)^2}. \quad (4)$$

This definition uses the spacecraft axis system where yaw is deviation in the ecliptic plane and pitch is deviation North and South of the ecliptic. Example values for a number of days are shown in Table 1 for both spacecraft. The HI-1 and HI-2 values are computed using Equation (4) for the centers of the fields of view at elongations of 14° and 53° respectively. These values show clearly the dramatic increase in roll fluctuations that occurred at the time that the gyros were turned off, there was also a substantial increase in pitch fluctuations and a smaller increase in yaw fluctuations at the same time. The large increase in roll fluctuation is to be expected as the roll is sensed only by the star trackers, which have a slower feedback than the guide telescope which senses pitch and yaw only. Immediately after the resumption of full operations in November 2015, following superior conjunction, there was a large increase in roll fluctuations in STEREO-A, to about 100 arcsec, but this was resolved within a few days. On 24 Feb. 2016, a revised pointing control algorithm was uploaded to STEREO-A with the intent of improving the control of the roll fluctuations. As can be seen in the final row of Table 1, this has resulted in a significant improvement of pointing performance with the roll variations on a 1 minute timescale being roughly half those shortly before conjunction, but still much higher than they were while the gyros were in use.

To illustrate the effect of these pointing fluctuations on the response of the instruments to stars we plot the daily medians of the ratio of the stellar count rates to their median values over the interval from the start of science operations until the gyros were turned off in Fig. 7. (Only the values from mid-2012 until the start of reduced data operations leading up to superior conjunction are shown). In Table 2 we show the median value and interquartile ranges of the apparent gains for three 200 day intervals: just before and just after the change to gyroless attitude control, and also after the upgrade of the gyroless control algorithms in February 2016. All of the apparent gain values are relative to their medians over the science phase of the mission prior to the gyro switch-off. In Fig. 8 we show the histograms of the gain for each instrument for the same intervals as in Table 2. From these plots and numbers it is very clear that there was a drop of about 5% in the apparent gain of all instruments (albeit smaller in HI-2B) when the gyros were turned off. There is also an increase in the scatter of the values, by about a factor of three for the HI-A cameras and rather less than that for HI-B. The increased scat-

Table 1. RMS pointing fluctuations on a 1 minute timescale, in arc seconds.

Date	STEREO-A					STEREO-B				
	Roll	Pitch	Yaw	HI-1	HI-2	Roll	Pitch	Yaw	HI-1	HI-2
9 Apr. 2008	2.16	2.09	0.41	2.13	2.18	1.87	2.00	0.47	2.04	1.98
19 Jul. 2013	0.80	1.60	0.61	1.68	1.31	1.20	0.67	0.56	0.90	1.18
10 Apr. 2014	29.19	9.25	1.17	11.48	23.99	35.84	10.50	1.04	13.42	29.33
15 Jan. 2016	31.58	5.74	0.85	9.49	25.47				<i>No Data</i>	
17 Jul. 2016	12.89	5.60	0.64	6.29	10.85				<i>No Data</i>	

ter is probably the greatest concern for stellar measurements. The February 2016 revisions to the attitude control on STEREO-A resulted in a marked improvement over the original gyroless performance with only about a 2% reduction in gain and a factor of two increase in scatter compared with the times when the gyros were in use. We have also investigated the variation of the gyroless gain with stellar magnitude, but do not find any significant trend.

The high scatter throughout the mission in HI-1B, and also the fluctuations of other parameters illustrated in this section have their origin in movements of the HI-1B focal plane assembly relative to the spacecraft. These will be considered in Sect. 4.2, and will be ignored in this section.

The positional shifts of the sky image on the CCD detector between successive exposures caused by the increased pointing jitter are typically considerably smaller than the size of a CCD pixel. None-the-less the shift of the stellar centers between successive exposures is such as to cause a substantial enhancement of the number of pixels flagged as cosmic rays. The trends in the cosmic ray counts are shown in the left hand column of Fig. 9. Note that the first exposures of each sequence are excluded from the computations of hit rates shown here, as the longer gap to the previous exposure means that the hit rates in those exposures are much higher than for other exposures. The extra hits are due to the effects of spacecraft orbital motion and is discussed in Sect. 4.3. The cosmic ray counts show an increase in the number of hits flagged in all cameras at the time of the transition to gyroless attitude control. This change (with the exception of HI-2A) is comparable with other excursions in the hit rate (which are caused by real variations of particle flux). As a more robust indicator of pointing-driven particle hit excess, we use the parameter Δ , first used by Tappin, Eyles, & Davies (2017), which is defined as:

$$\Delta(P, n) = \frac{P_{0.75}}{\text{mmm}(P_{0.25}, n)} - 1, \quad (5)$$

where P represents the number of pixels scrubbed in each exposure of an image, P_x represents the x th fractile of

those counts and $\text{mmm}(P_x, n)$ represents the background of P_x (computed using the `mmm` routine from the SolarSoft DAOPHOT suite) from the n images before and after the current image. We set the image window n to correspond to five days at the nominal image cadence. Thus for HI-1 we used a ± 180 image window, while for HI-2 we used a ± 60 image window. Δ is in effect a measure of the spread of the cosmic ray counts within the exposures making up an image, normalized to the typical counts on a timescale of 5 days. The values of Δ are shown in the right hand column of Fig. 9. These plots of Δ show a much clearer distinction between the gyro-controlled attitude interval and the gyroless interval than the hit rates on their own. We interpret this to mean that following the transition to gyroless attitude control, there are shifts between successive exposures that cause significant flagging and “correction” of pixels and that there is considerable variation in the level of this between exposures, thus increasing the spread of hit counts more than the absolute hit counts.

In Fig. 10 we show the correlation between Δ and the median apparent gain for each science image. From these correlations it is clear that at high Δ there are two populations of images, those with reduced gain, and those whose gains are close to unity. The high Δ images with gains close to unity, which mostly occurred while the gyros were still in use, appear to be those where there were actual particle events in progress. The fits shown in Fig. 10 are L1-norm fits to the points after the high- Δ high-gain images are excluded. While there is a very clear anticorrelation between Δ and the apparent gain in those images with reduced gain, there is also a wide scatter which means it is unlikely to be possible to use Δ to make an adjustment to the camera gain, at least not with sufficient accuracy to be useful for photometric studies.

4.2. HI-1B shifts

As we have noted above, HI-1B shows a much larger scatter of apparent gain values than the other imagers (Figs. 7 and 10), and also has numerous spikes in Δ (Fig. 9c). This was true even during the phase of the

Table 2. Medians and interquartile ranges of the apparent gains of the HI instruments for 200 day intervals before and after the switch to gyroless operation, and since the pointing revisions in February 2016.

Instrument	Before		After		Recent	
	Median	IQ	Median	IQ	Median	IQ
HI-1A	0.999	0.009	0.961	0.036	0.981	0.017
HI-1B	0.998	0.025	0.967	0.059	<i>No Data</i>	
HI-2A	0.997	0.013	0.941	0.039	0.982	0.028
HI-2B	0.998	0.019	0.992	0.028	<i>No Data</i>	

mission when spacecraft pointing was sensed by the gyros. Also, HI-1B shows large numbers of high- Δ low-gain images while the gyros were still in use, while the other imagers do not (Fig. 10b). The apparent gain variations of HI-1B are shown in more detail in Fig. 11, which shows daily values on a scale that allows the details of the fluctuations to be seen. From this it can be seen that the scatter in apparent gain is dominated by dropouts in gain lasting from one to several days. Early in the mission (up to the start of 2009) these tended to line up with the spacecraft momentum dumps. These early dips typically had longer duration and were somewhat deeper than those later in the mission. The minima in apparent gain match up to the peaks in Δ for HI-1B seen in Fig. 9.

It has long been known that there are shifts in the pointing of HI-1B relative to the spacecraft axes (Brown, Bewsher, & Eyles 2009; Davis et al. 2012; Tappin, Eyles, & Davies 2017), and it therefore seems logical to determine whether these shifts are correlated with the gain dropouts and Δ peaks. Tappin, Eyles, & Davies (2017) showed that the range of movement of HI-1B pointing relative to the spacecraft pointing approximates a truncated circle. In Fig. 12 we show a 2-D histogram of the pointing corrections made in converting the Level-0 images to Level 1 for each science image returned by HI-1B, using the pointing alignment method described by Brown, Bewsher, & Eyles (2009). In this figure we have removed the effects of an update in the spacecraft pointing parameters uploaded on 18 Jun. 2008, by adjusting the corrections from before that date to match the updated spacecraft pointing.

This representation shows very clearly the nearly circular distribution of the pointing corrections, with an excluded region in the lower right. It is quite evident from this that there is a certain amount of slack in some part of the HI-1B camera mounting assembly. The concentration of points towards the edge of the distribution of points shows that the assembly normally settles against the edge of the region of accessibility, and only transiently crosses the interior of the region. The dashed curve in Fig. 12 shows the 95th percentiles of

the radial displacements in 5° bins of angle (relative to an approximate center of the distribution), the circle is a fit to those percentiles, excluding the marked sector. These show that the play in the mounting is almost circular. We have examined the pointing distributions for the other imagers, and find that if there are any shifts in their pointing relative to the spacecraft these are very small.

To illustrate the behavior of HI-1B across a momentum dump we show the apparent gain of HI-1B across the momentum dump on 23 Sep. 2008 (day 267) in Fig. 13; along with a number of other parameters relating to the apparent cosmic ray counts and the pointing. The first feature that is apparent is that the gain dropout lasts for several days and begins well before the momentum dump, which means that this cannot be a direct response to the momentum dump itself (e.g. destabilization caused by the thruster firing). From Fig. 13b and c, it is very clear that the gain dropouts correlate very well with the total cosmic ray counts and also the cosmic ray spread parameter Δ (Equation 5). The dropouts and times of high Δ do not match with the major jumps in pointing (Fig. 13d), although the interval of high cosmic ray counts begins at such a jump. Rather they match up with the times following the jumps where there are small fluctuations in the pointing, which are visible as the small-scale structure in Fig. 13d. To further characterize this we define a pointing jitter as:

$$J = \left((\delta x - \text{median}(\delta x, 15))^2 + (\delta y - \text{median}(\delta y, 15))^2 \right)^{\frac{1}{2}}, \quad (6)$$

where δx and δy are the pointing adjustments of the image and $\text{median}(x, n)$ is an n -point running median of x . This is plotted in Fig. 13e. From this and other similar intervals, we find that when a major shift occurs close to a momentum dump, the pointing correction takes much longer to settle back to a stable state than at other times, as can be seen both from the small excursions on the trace in Fig. 13d from about day 260 to 272 and the values of J in Fig. 13e. Indeed at some dumps there is enhanced jitter and a gain dropout with no major shift of pointing. It is also clear that the pointing jitter is

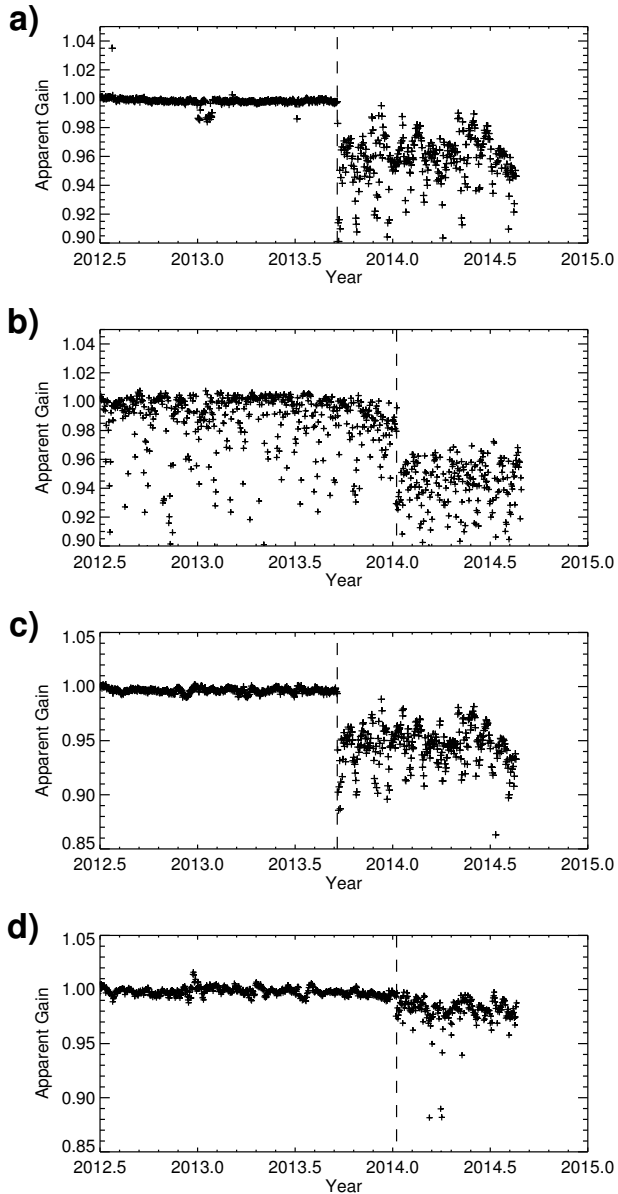


Figure 7. Gain trends for all of the HI instruments from mid-2012 until the end of pre-conjunction data. a) HI-1A, b) HI-1B, c) HI-2A and d) HI-2B. Each point is a daily median of the ratio of the measured stellar count rate to the star’s mission-long median. The vertical dashed lines show the times of the switches to gyroless pointing control.

well-correlated with Δ which is in turn well-correlated with the apparent gain.

The purpose of the momentum dumps is to keep the spin rates of the attitude control reaction wheels within safe operating limits (Driesman, Hynes, & Cancro 2008), and thus the wheels will have high spin speeds close to momentum dumps (and a direction reversal at the dump), it therefore seems logical to look to the reaction wheel speeds as the ultimate driver of these dips. The

reaction wheel speeds are shown in Fig. 13f (STEREO reaction wheel speeds can be found in the converted spacecraft housekeeping files in the ancillary data section of the STEREO Science Center <http://stereo-ssc.nascom.nasa.gov/ancillary.shtml>). We find that when any reaction wheel is spinning faster than about 350 revolutions per second (rps), there is always small-scale instability in the pointing corrections, and a correspondingly elevated level of Δ . The relation between reaction wheel speed and Δ (and by implication the HI-1B pointing stability) is clearly illustrated by the plot in Fig. 14, which also shows a clear resonance at about 170 rps, and weaker signals near 100 and 270 rps. In a more qualitative way the relation can be seen in Fig. 13 by comparing the behavior of the various parameters after the large shift on day 260 with those after day 285.

At times other than around the momentum dumps, the settling period after major shifts appears to be increased when the reaction wheels are spinning fast. Our interpretation of this is that vibrations from the reaction wheels are propagating into the HI structure, and when the wheel speed exceeds about 350 rps are sufficient to cause the HI-1B structure to become unstuck, at other times the vibrations may be sufficient to prevent it settling quickly after it has been dislodged by some other cause.

As is seen in Fig. 11, the long gain dips around the momentum dumps only occur up to the beginning of 2009. At this time the frequency of the momentum dumps was increased, such that the typical maximum wheel speed was lowered to about 300 rps (from 350–400). Gain dips do occur in later data and in some cases they are associated with momentum dumps. However in these cases the gain dip appears to follow the momentum dump suggesting that the release is caused by the thruster firing and then the relatively high wheel speed leads to a slow resettling. Other dips are most likely initiated by interplanetary dust as conjectured by Davis et al. (2012), with their duration influenced by the reaction wheel speeds.

4.3. Orbital motion

The third (and final) motion that can cause stellar signal to be misidentified as particle hits is the orbital motion of the spacecraft around the Sun. This is the smallest of the three mechanisms, but also the most ubiquitous and the most difficult to quantify.

That this effect is important can be judged from Fig. 15 which shows the cosmic ray counts for the first exposure of each science image. Here the cosmic ray counts are dominated by a term that varies on a timescale of about half the spacecraft orbital periods

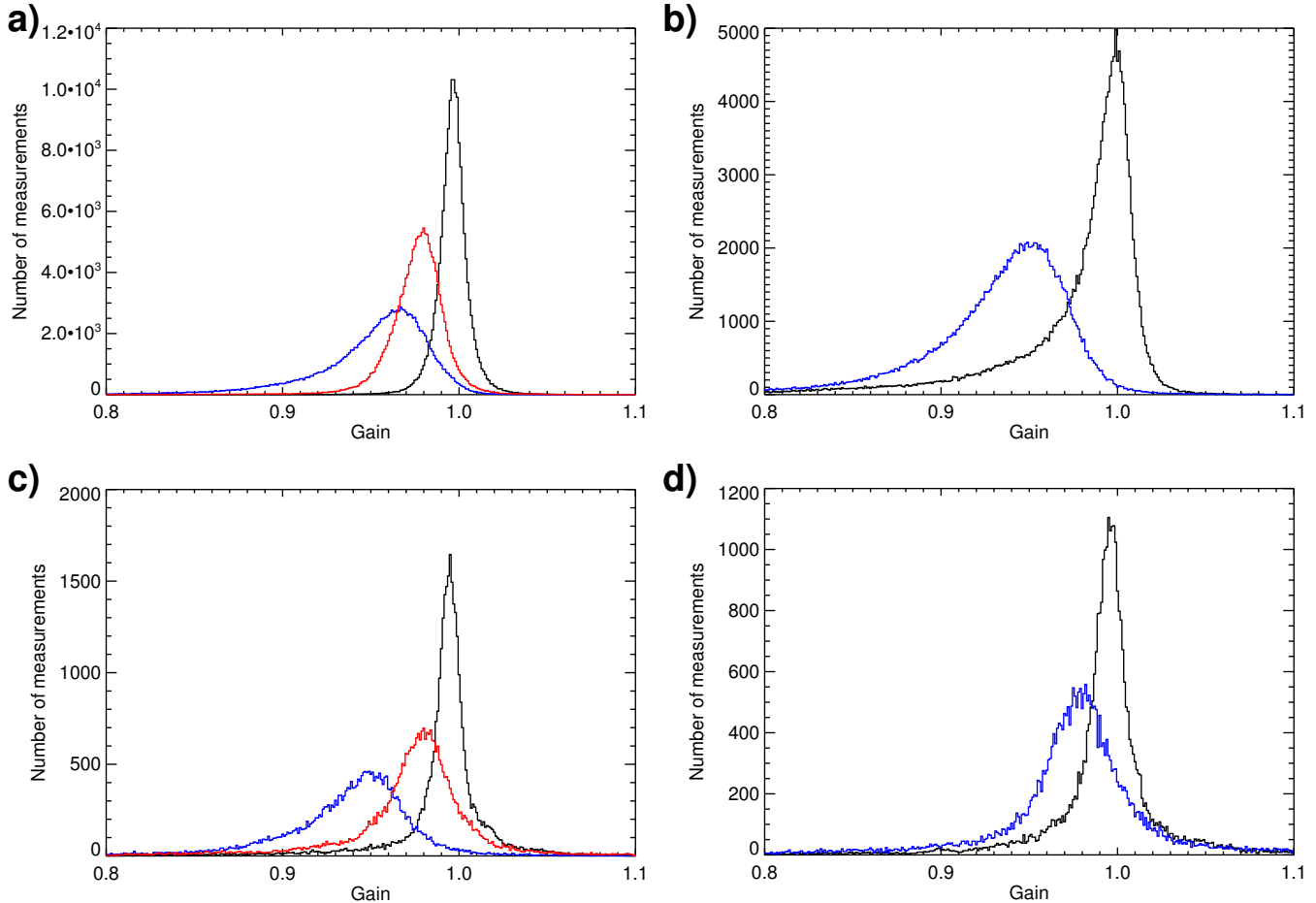


Figure 8. Histograms of the scatter of individual stellar gain measurements for all four HI instruments. a) HI-1A, b) HI-1B, c) HI-2A and d) HI-2B. The black traces are for a 200-day interval immediately prior to the gyro switch-off, the blue traces are for 200 days after the switch-off, and the red traces (HI-A only) are for 200 days after the improved pointing correction was introduced. All gains are relative to the median of the whole gyro-controlled phase of the science mission. The bin size for the histograms is 0.001 in all cases.

around the Sun (345 and 389 days for A and B respectively). This is in contrast to the later exposures of the integration where short-term variations due to space weather events (as well as the other effects discussed in this paper), and long-term variations driven by the solar cycle dominate up to the time when the gyros were turned off (Fig. 9).

The number of hits in the first exposures correlates very well with the galactic latitude of the center of the camera field of view, as is clearly shown by Fig. 16. This would imply that the hit rate is driven by the number of stars in the field.

There have not, to date, been any sequences of full-resolution single exposures returned at the normal cadence with standard exposure times with which it would be possible to directly investigate the effect. It is therefore necessary to simulate the effects of the tracking of the field of view across the sky from exposure to ex-

Table 3. Summary of the shifts between exposures used to simulate the effects of orbital motion.

Imager	First Exposure			Remainder		
	Min.	Arcsec	Pixels	Min.	Arcsec	Pixels
HI-1	10	25.0	0.71	1	2.5	0.071
HI-2	21	52.5	0.40	1	2.5	0.020

posure, using the available single-exposure images and interpolation. A simplified version of this was done for HI-1 by Tappin, Eyles, & Davies (2017), who concluded that the effect on the measured brightnesses of stars in HI-1 was of the order of 1%, except for the brightest stars. Here we carry out the analysis in more detail, and also examine the HI-2 imagers.

For the simulations presented here, we have assumed an orbital speed of 2.5 arcsec per minute (1° per day). While this is not exact as STEREO-A moves at an aver-

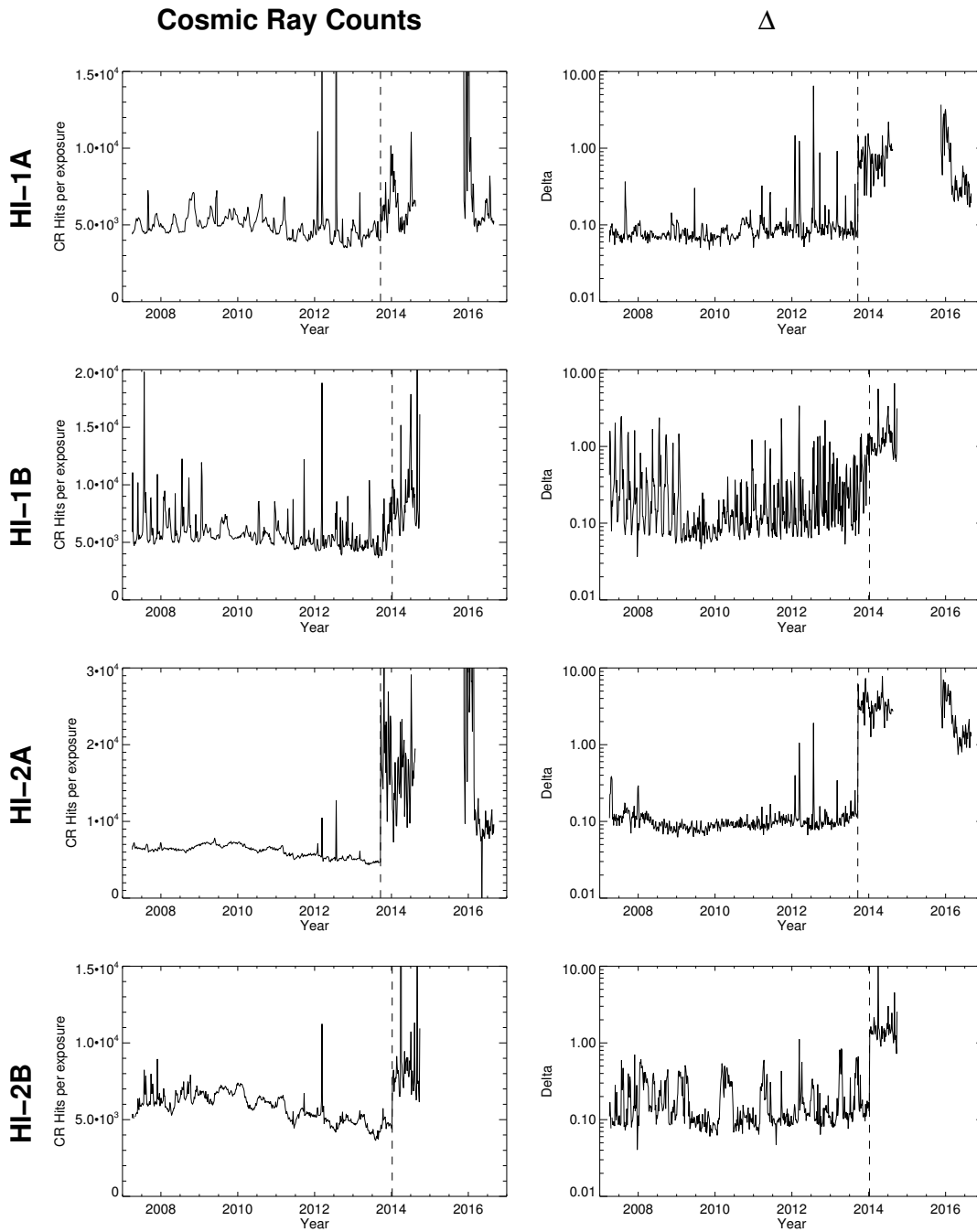


Figure 9. 5 day medians of cosmic ray (CR) parameters for the science phase of the STEREO mission up to September 2016. Left Column: CR counts per exposure from exposures other than the first of each accumulation sequence, Right column: the values of Δ . Row 1: HI-1A, Row 2: HI-1B, Row 3: HI-2A and Row 4: HI-2B. The vertical dashed lines in all panels show the times of the switch to gyroless operations.

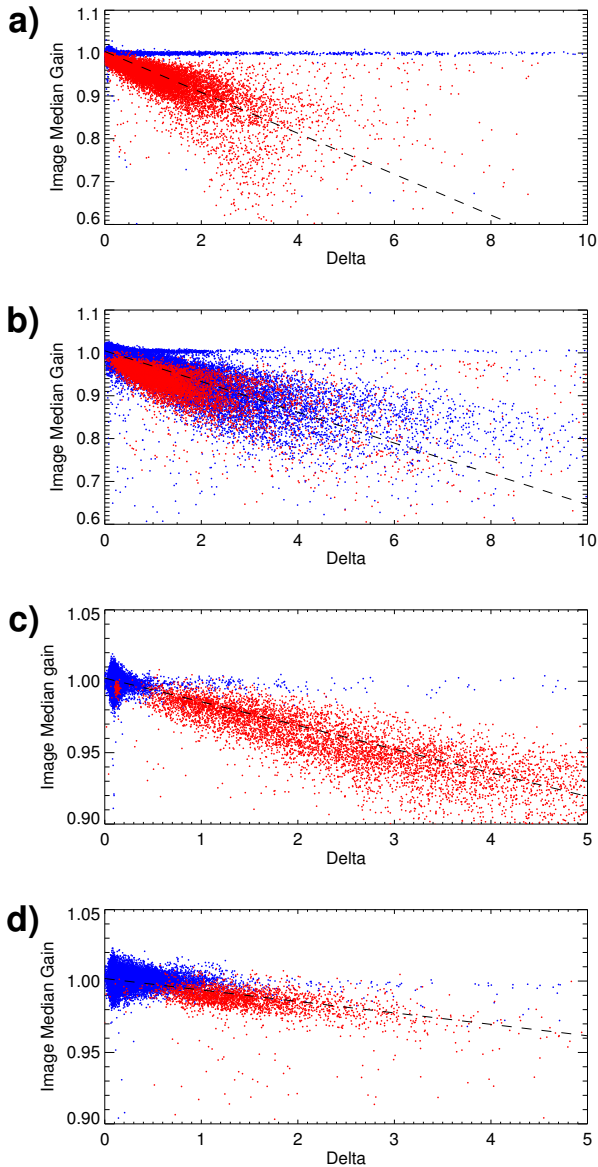


Figure 10. Correlations of the image median gains with Δ . a) HI-1A, b) HI-1B, c) HI-2A, and d) HI-2B. Points before the gyros were turned off are shown as blue symbols, and those after that date as red symbols. The dashed lines are fits to the points (excluding the high-gain, high-delta region). Gains are relative to the gyro-controlled median value. Note that the HI-1 and the HI-2 plots have different scales.

age of 2.6 arcsec per minute, and STEREO-B at 2.3 arcsec per minute (with a small but non-trivial variation due to the ellipticity of its orbit), they are sufficient to give a good estimate of the effects of orbital motion on the interaction between stellar images and the cosmic ray scrubbing algorithm. Since the exposure sequences are separated by a gap of 10 and 21 minutes for HI-1 and HI-2 respectively (Eyles et al. 2009), we need to

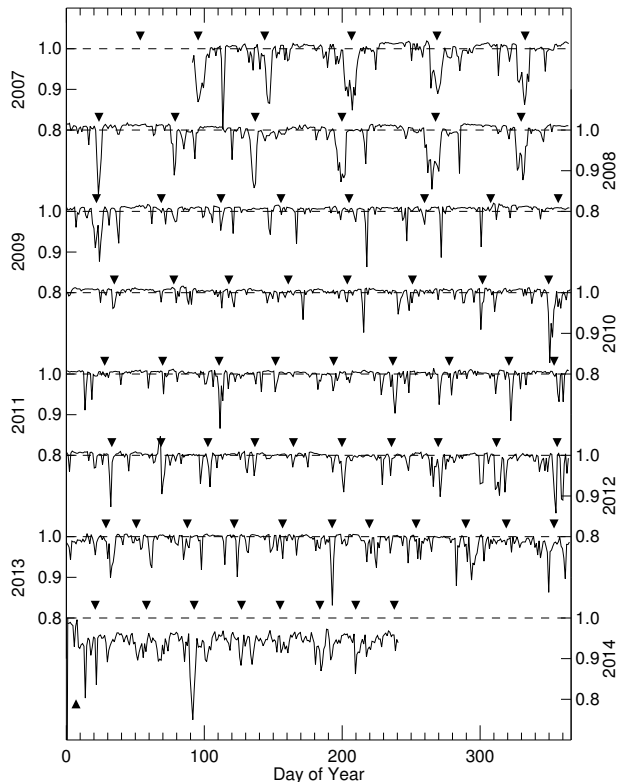


Figure 11. Apparent gain of HI-1B throughout the science phase of the mission (1 Apr 2007 to 1 Oct 2014). The axes for successive traces are on alternate sides of the plot, with the year indicated alongside. As in Fig. 7, the values are daily medians of the ratio of the stellar count rates to their mission median value. The horizontal dashed lines show the unit gain level for the corresponding traces. The downward-pointing black triangles show the times of spacecraft momentum dumps. The upward-pointing triangle below the 2014 trace shows when the gyros were turned off.

consider the first exposure in each image sequence separately. This combination of the orbital speed and exposure cadence gives the pixel shifts listed in Table 3.

To simulate the effects of the scrubbing algorithm (Equation 1) on an exposure we use the following procedure:

1. Take a full-resolution, single-exposure image.
2. Generate a simulated previous exposure by shifting the image to the left by the required number of pixels (from Table 3). This is done row by row using the INTERPOL routine in IDL with a spline interpolation. This does not take account of the variation of plate scale across the field of view (Brown, Bewsher, & Eyles 2009; Tappin, Eyles, & Davies 2015), nor of any motion of the stellar images in the CCD Y direction, but both of these

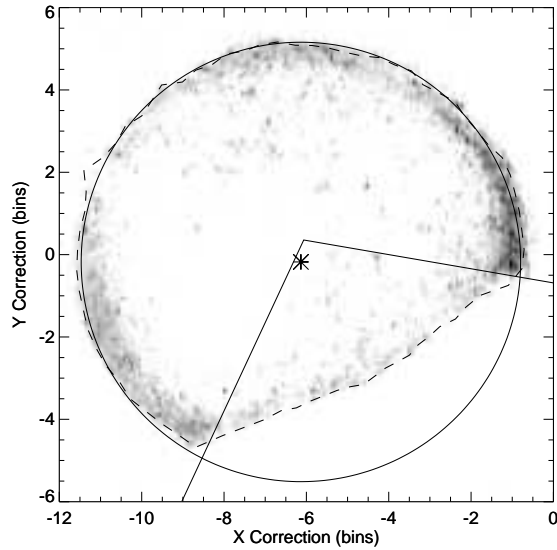


Figure 12. Pointing corrections from Level-0 to Level-1 images for HI-1B for the science phase of the mission. The data are shown as a 2-D histogram with square-root scaling and adjusted to post 18 Jun. 2008 spacecraft pointing parameters. The dashed line shows the 95th percentile radial displacement from an approximate center of the distribution. The circle is a fit to those values excluding the flattened sector in the lower right. It has a radius of 5.337 bins and is centered at $(-6.133, -0.178)$.

are small compared with the stellar motion in the CCD X direction. In addition the F-corona and any actual particle hits are shifted along with the stellar images. This technique does however appear to be a sufficiently good approximation for this analysis.

3. Generate a scrubbed version of the current exposure by applying Equation 1 to the original image and the simulated previous image.

It should be noted here that while this procedure provides a good simulation of the effect of the scrubbing algorithm on the stellar responses, it cannot simulate the effectiveness of the scrubbing algorithm (or of any alternative) in removing particle hits as real particle hits are propagated back into the simulated previous exposure by the interpolation procedure along with the stars.

To determine the effects of the scrubbing on the measured count rates in the science images, we then rebin both the original and the scrubbed exposures to 1024×1024 bins. Since there are known to be systematic offsets in the Level-0 pointing information that correspond to a few bins in the image plane (Brown, Bewsher, & Eyles 2009), we use the header informa-

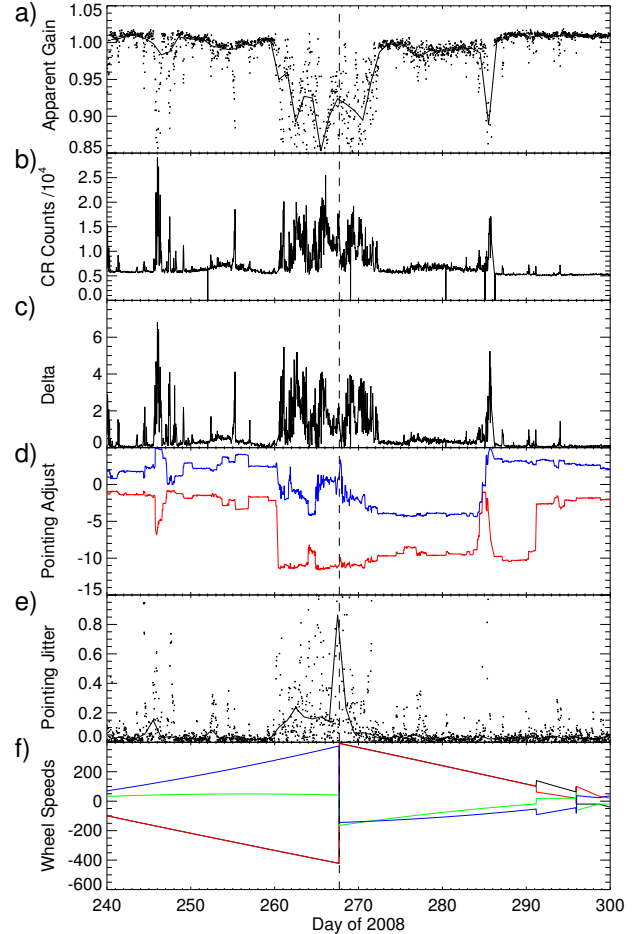


Figure 13. Details of the HI-1B gain dropout associated with the momentum dump on 23 Sep. 2008 (day 267). a) The apparent gain, the dots show the values for individual images and the line is a daily median value. b) The median number of hits recorded in each “normal” exposure in each image. c) The Δ parameter. d) The pointing adjustments made between the Level-0 and Level-1 images, in units of image bins, red line = CCD X-direction, blue line = CCD Y-direction. e) The jitter in the pointing (from Equation 6), the dots show J values for individual images and the line is a daily median. f) The speeds of the spacecraft attitude control reaction wheels, black = wheel 1, red = wheel 2, green = wheel 3, and blue = wheel 4. The vertical dashed line running through all of the panels shows the time of the momentum dump.

tion from the corresponding Level-1 images (which have been corrected by matching star locations in the images with catalog positions using the procedure described by Brown, Bewsher, & Eyles (2009)) to determine the locations of stars from the SKY2000 catalog (Myers et al. 2001). For each star brighter than magnitude 9.0 (HI-1 A and B), 7.0 (HI-2A) or 6.0 (HI-2B) that lies in the field of view, we compute the integrated counts in

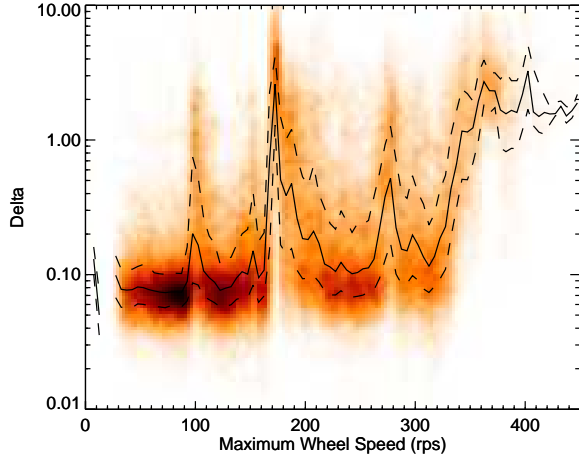


Figure 14. The relationship between Δ and maximum reaction wheel speed for HI-1B for the interval up to 7 Jan. 2014. The solid black line is the median of Δ in 5 rps bins, the dashed lines show the upper and lower quartiles. The color map is a 2-D histogram of the Δ values.

the rebinned images, using either the aperture photometry method (Tappin, Eyles, & Davies 2017) for HI-1 or the descents method (Tappin, Eyles, & Davies 2015) for HI-2. Since only the relative counts in the scrubbed and unscrubbed exposures are important in this study, we do not need to limit our attentions to the stars that satisfy the calibration-star criteria described in those works.

This procedure was applied to all of the suitable exposures taken in 2009 and 2012. The results for these two years are very similar, therefore we have not extended the analysis to other years and we present only combined results here. In Fig. 17(a,b) we show the median ratio of the counts derived from the scrubbed and unscrubbed exposures as a function of stellar magnitude, Fig. 17a is for simulations of the first exposure of a science image, and Fig. 17b is for the remaining exposures. In Fig. 17c we combine the values from panels a and b, taking account of the fact that HI-1 images are the sum of 30 exposures and HI-2 images are the sum of 99 exposures. From this we see that the net reduction of count rate for the fainter stars in HI-1 is about 1%, due entirely to the first exposure of the sequence, and this increases to about 3% for stars brighter than about magnitude 5.0. In HI-2, where the inter-exposure shifts are a smaller fraction of a pixel, the effects are much smaller. For HI-2A the effect ranges from about 0.1% for the fainter stars up to a maximum value of about 0.3% for stars brighter than magnitude 3.0, while for HI-2B which has a much larger PSF, and thus smaller intensity gradients on the CCD, the effects are negligible.

In the HI-1 simulations, there is a minimum in the ratio of the counts for the first exposure case at about magnitude 5.5 (Fig. 17a). We do not currently have an explanation of this, but we suspect that it is more likely to be an artifact of the simulations than a real effect, as it occurs more than a magnitude fainter than the level at which saturation starts to become important.

We have investigated the variation of orbital-motion scrubbing as a function of location on the CCD. In the HI-1A detectors, the dominant effect (Fig. 18a and b) is the intensity of the F-corona, which reduces the significance of the changes in measured counts when it is high by adding total signal but not affecting the change in signal, thus there is significantly less scrubbing of stellar images at small elongations. HI-1B (not shown) is very similar. For HI-2A (Fig. 18c and d) the increase in PSF diameter in the outer parts of the field of view reduces the change of measured count and thus the scrubbing. For HI-2B (also not shown) the effect is similar but at a much lower level.

We also investigated whether the location of the star within the pixel had any effect on the likelihood of it suffering scrubbing. For most cases we did not find any significant effects, however for the HI-1s in the first exposure of the sequence, there is a reduction of 3 to 5% in the amount of scrubbing when the star is near to the boundary of the pixel at the midpoint time of the exposure compared with when the star is near the center of the pixel (Fig. 19). This is in broad agreement with the changes in intensity predicted from analyzing a single averaged HI-1 PSF.

Since this affects only the first image of the accumulation, the effect on the total measured count rate in a science image will only be a noise term of about 0.1% in the measured count rate for a star.

5. PROJECTION

The projection of the HI instruments is normally represented by the azimuthal perspective (AZP) projection in which the radial distance (R) from the center of the image is related to the angle to the optical axis (α) by the relationship:

$$R = F_p \frac{(\mu + 1) \sin \alpha}{\mu + \cos \alpha}, \quad (7)$$

where F_p is the paraxial focal length and μ is a distortion parameter (Calabretta & Greisen 2002). The application of this projection to the HI cameras is however a purely empirical fit (Eyles et al. 2009). In their determination of the HI-2 calibration parameters Tappin, Eyles, & Davies (2015) found a small radial deviation of the measured locations of the stars from the computed positions.

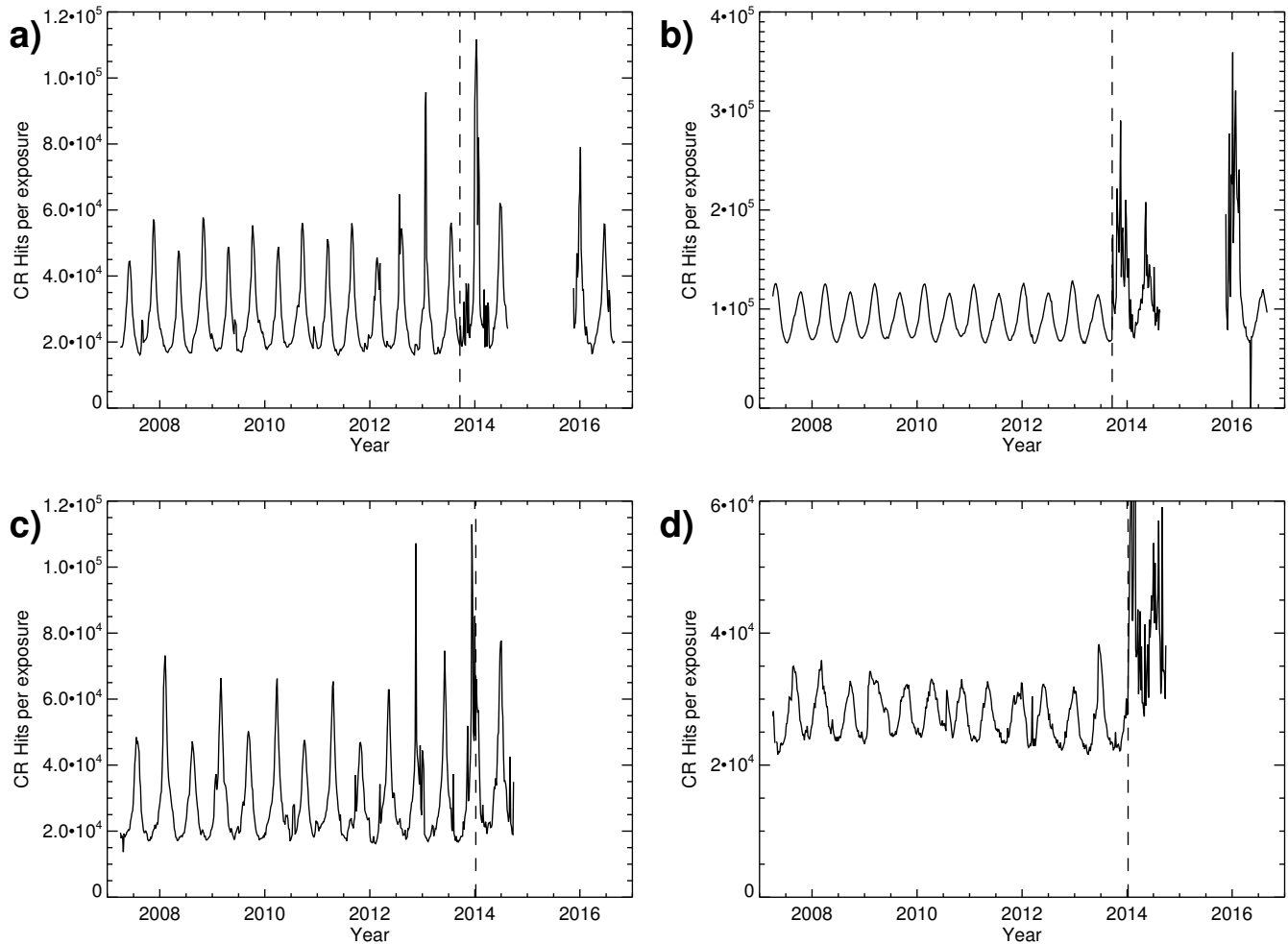


Figure 15. Cosmic ray counts per exposure for the first exposure of each science image. a) HI-1A, b) HI-2A, c) HI-1B and d) HI-2B. As in Fig. 9, the vertical dashed lines mark the transition to gyroless attitude control.

In Fig. 20 we show the radial displacements of measured stellar positions from those computed using the best-fit AZP parameters for all of the HIs. This shows that for HI-1, AZP is a very good fit, with no measurable systematic deviations from the nominal projection. For HI-2 there is a clear systematic variation, but it only becomes large beyond the nominal circular field of view. In all cases, the deviation within the usable region of the image is small compared with the PSF, and so does not present a significant risk of mis-identifying stars.

6. DISCUSSION

6.1. *Astronomical implications*

At first sight, the foregoing analyses might be taken to imply that using measurements from the STEREO-HI instruments for astronomical science is pretty much a lost cause. This is, however, far from the truth. All instruments have their peculiarities and flaws, in general the designers and constructors will optimize the charac-

teristics of the instrument to maximize the return from its primary mission. In this the STEREO-HI instruments are no exception, their primary mission is to observe CMEs and other diffuse structures as they propagate through the heliosphere from the edge of the field of view of conventional coronagraphs to the region of 1 AU from the Sun (Howard et al. 2008; Eyles et al. 2009). These characteristics impose on the instruments a number of requirements, including:

- A large field of view.
- A consistent sequence of observations, with several images per day.
- Stable photometric performance, primarily for diffuse sources.
- A region of observation close to the ecliptic plane.

All of these characteristics also make the STEREO HIs a valuable suite of instruments for monitoring bright stars

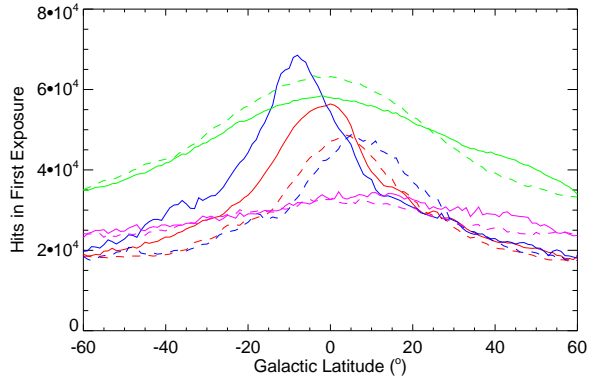


Figure 16. Plots of the numbers of particle hits recorded in the first exposure of the images from the HI cameras plotted as a function of the galactic latitude of the center of the field of view. Each trace shows the median number of hits from all science images up to 11 Sep 2016 in 1° bins. Red: HI-1A, Blue: HI-1B, Green: HI-2A divided by 2, Magenta: HI-2B. The solid lines are for longitudes towards the galactic center and the dashed lines are towards the anti-center.

over the medium to long term, something which is seldom possible with campaign-based telescopes. They also observe in a region of the sky seldom targeted by dedicated survey instruments.

That we are able to isolate and characterize the various effects described in this article, is in itself a testament to the overall performance of the HI instruments themselves. None-the-less, to obtain useful science, steps must be taken to exclude affected intervals or to mitigate the effects which we have discussed in the foregoing sections.

6.1.1. Saturation effects

The saturation of pixels imposes a limit on the magnitude of star for which the response of the cameras can be considered to be linear. For the HI-1 instruments this occurs at about magnitude 4.7 with some variation as a function of elongation. For HI-2A near the field center the critical point is also at about this level, while for HI-2B the larger point spread function means that there are no saturation effects for stars fainter than magnitude 3.5. As is clear from comparing the Level-0 single exposure image peak rates with the Level-1 science image integrated rates (Figs. 5 and 6, and the supplementary files), although there is a significant deviation from linearity for bright stars the response in the science data does not completely level out. Therefore it is still possible to detect variability in the bright stars even if its quantification becomes less reliable.

It should however be remembered that the saturation limit does vary across the field of view. For HI-1 the dominant driver of this is the presence of a strong F-

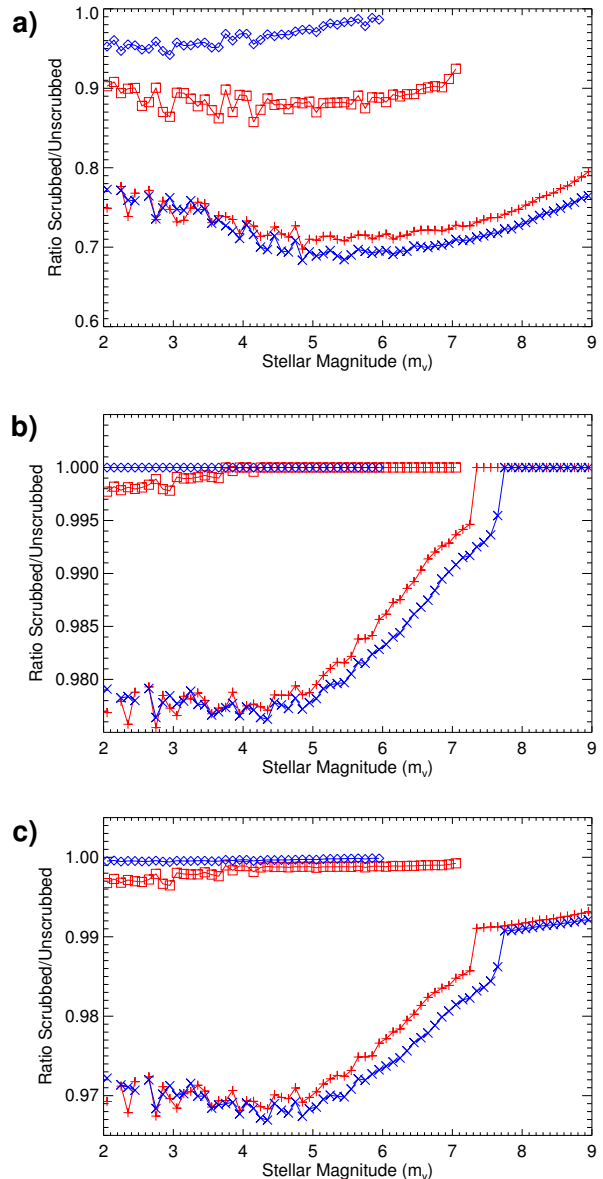


Figure 17. Ratios of integrated stellar counts in scrubbed and unscrubbed single exposure images from 2009 and 2012. a) For first exposures (i.e. previous exposure 10 or 21 minutes before). b) For normal exposures (i.e. previous exposure 1 minute before). c) Combined effect. + symbols for HI-1A, \times symbols for HI-1B, open squares for HI-2A and open diamonds for HI-2B. HI-A symbols are red and HI-B are blue.

coronal signal which reaches about 60% of the saturation level close to the Sun, thus the saturation limit for stars is about one magnitude fainter near to the Sun than it is far from it. Hence, for stars close to the saturation limit, a gradient in measured count rate is expected as the star moves across the field of view.

For HI-2 the effect of the F-corona is much less significant, but two factors combine to raise the saturation

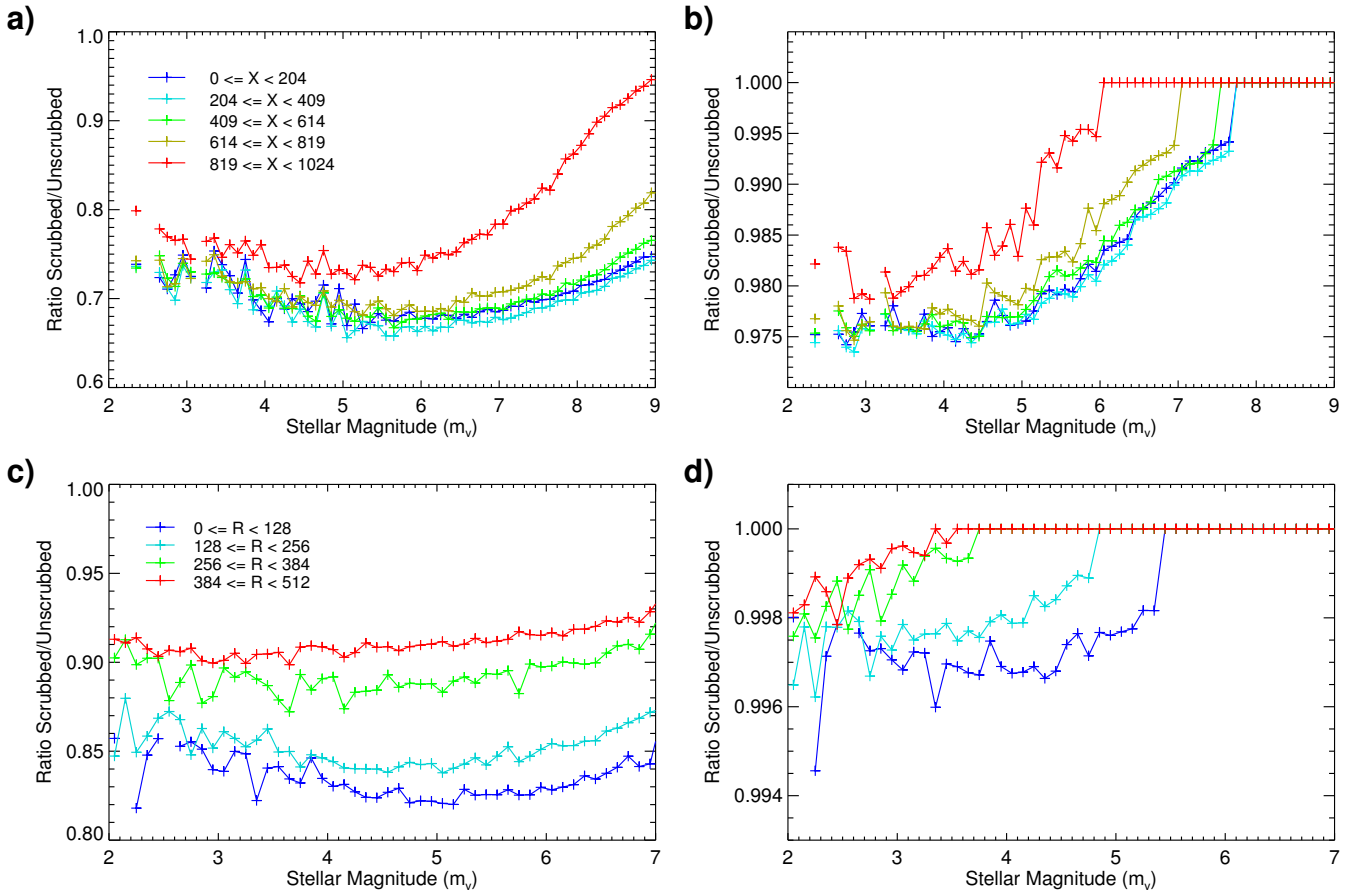


Figure 18. Ratios of integrated stellar counts in scrubbed and unscrubbed single exposure images from 2009 and 2012 as a function of location on the CCD. a) HI-1A first images, b) HI-1A normal images, c) HI-2A first images and d) HI-2A normal images. For HI-1A the five zones covering the central band ($341 \leq Y < 682$) from Fig. 3a are shown. For HI-2A all four radial zones from Fig. 3b are shown.

limit towards the outer edges of the field of view. Firstly the PSF becomes larger far from the center of the field, thus lowering the peak count rate for a given integrated count rate, and secondly near the edge of the field the large-scale flat field reduces the actual sensitivity by a substantial factor (Tappin, Eyles, & Davies 2015). As a result of these two effects, the saturation limit is almost two magnitudes brighter at the edge of the field of view than at the center.

For the vast majority of the stars observable by the HIs, those fainter than magnitude 5, there is no saturation. Of the approximately 4300 stars of $m_v < 10.0$ which pass through the HI-1 fields, only 27 are brighter than $m_v = 5.0$. For those very few brighter than that, variability and outbursts would still be detectable as the integrated counts always include many unsaturated pixels, but linearity of response can no longer be relied upon.

It is also worth noting here that although the effects of the F-corona (HI-1) and of the variable PSF and flat field (HI-2) on the maximum counts of stars is large, the

combination of the summing and background removal in the photometry algorithms, and the flat field corrections applied to Level-1 images mean that for stars that are not saturated the measured count rate is stable across the field of view.

6.1.2. Cosmic ray scrubbing

The effects of false positives in the cosmic ray scrubbing are more serious than those of saturation for astronomical uses of the HI data as they affect a much wider range of stellar magnitudes.

The first and most obvious step for handling the reduced gain due to the interaction of pointing instability with the cosmic ray scrubbing is simply not to use data from the affected intervals, i.e. only use HI-A data up to 17 Sep. 2013 and HI-B data up to 6 Jan. 2014 (and avoid times of high Δ for HI-1B). This may indeed be the only realistic option for high-precision absolute photometry.

However, the gain variations arising from the gyroless attitude control and from the HI-1B shifts are both due to movements of the instrument pointing. This means

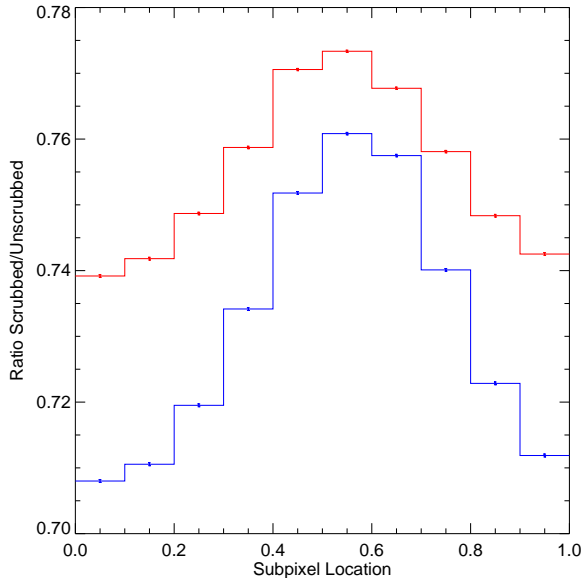


Figure 19. Variation of the effects of cosmic ray scrubbing on stellar response for the first exposure of the image as a function of the subpixel location of the star in the X-direction. Red: HI-1A, and Blue: HI-1B. A subpixel location of zero corresponds to the center of a pixel in the “current” exposure.

that all of the stars in the field of view will be affected similarly. It is therefore to be expected that stars that are close together will show correlated changes of count rate. Some examples of this are shown in Fig. 21. In all of these examples, it is clear that fluctuations in measured count rate on all time scales from single images up to the duration of the apparition match very well between the stars shown. This would imply that major gain fluctuations can be excluded by comparing observations of the target object with nearby stars that are known to be constant (or at least only slightly variable). This will both, identify severe dropouts such as those at the start of the HI-1A data in Fig. 21a, and on day 296 of the HI-2A data in Fig. 21b where the images are unlikely to be usable, and also allow a correction factor to be estimated. For studies using any of the cameras after the transition to gyroless operation, and for HI-1B throughout the mission, it is essential to use relative photometry with neighboring stars that are known not to be rapidly variable in order to get accurate determinations of variability.

The orbital motion of the spacecraft has a relatively small effect, at the 1–3% level, for HI-1 and much less than 1% for HI-2. This effect is magnitude-dependent, but time-stationary. Thus for any star it will introduce a scaling factor to the measured count rate. For HI-1 the scrubbing of stellar signals is reduced at small elongation

where the bright and spatially slowly-varying F-corona reduces the significance level of brightness changes due to stellar motions. However at elongations greater than about 10° the scrubbing of is almost constant (less than 0.2% change from 10° to the outer edge of the field of view). In the case of HI-2 there is more orbital scrubbing near the field center where the PSF is smaller, but the total scrubbing is so small that the changes across the field of view are unlikely to be detectable in real observations.

6.1.3. Projection effects

The nominal AZP projection is an excellent approximation to the true projection of the HI-1 cameras. For HI-2, there are measurable deviations, but they are not large enough to result in the mis-identification of stars. Thus the only necessary precaution is to use the image to precisely locate the star once its predicted location has been computed. It should here be noted that if the descents method of photometry (Tappin, Eyles, & Davies 2015) is used for HI-2 data, then this is done automatically.

6.2. Implications for future imagers

Since the only way to accurately calibrate a heliospheric imager once it is in space is by observing stars, these effects also have an impact on the ability to calibrate instruments, and for that reason it is reasonable to consider possible changes that could make future heliospheric imagers less susceptible to such problems.

There is little can be done to reduce the effects of saturation. For any useful spatial resolution, the intensity of bright stars will be many times greater than the radiance of the F-corona integrated over a pixel. Therefore to make a marginal gain in stellar performance (for a tiny minority of stars), several bits of potential radiance resolution for CMEs would be sacrificed, which is not a compromise likely to be attractive to the designers and primary users of a heliospheric imager. Defocussing the PSF (as was done (unintentionally) on HI-2B and (intentionally) on the Solar Mass Ejection Imager (Eyles et al. 2003)) to reduce peak counts has been found to cause as many problems as it solves.

The driver of all of the pointing-related gain drops in the HIs is the onboard cosmic ray scrubbing algorithm. Applying a particle-scrubbing algorithm and then summing on board is a necessity for any heliospheric imager operating beyond the confines of low Earth orbit, as in a single long exposure the number of energetic particle hits would lead to an unacceptable image degradation. The average hit rate is estimated to be $\sim 45\text{s}^{-1}$ for each CCD, (Eyles et al. (2009)), so for HI-2 the 99 minute integration

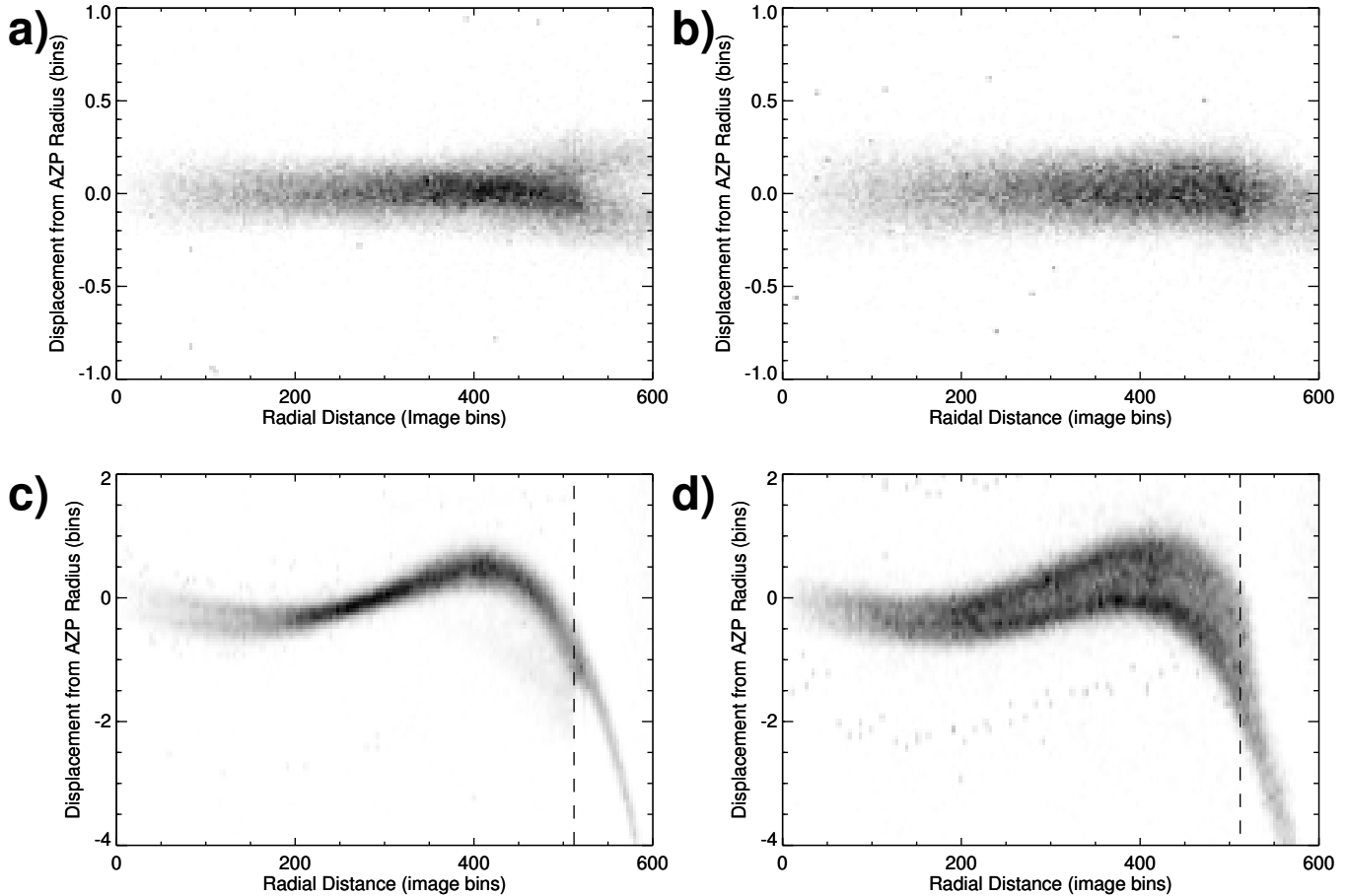


Figure 20. Radial deviations of the HI projections from the nominal AZP values. a) HI-1A, b) HI-1B, c) HI-2A and d) HI-2B. In each case the distortion is displayed as a 2-histogram. For the HI-2 plots, the limit of the nominal field of view is shown as a vertical dashed line.

would give about 4500 hits or about one bin in 200 affected, and many more when SEP fluxes are elevated. It is not possible to transmit all of the exposures to Earth with any reasonable telemetry allocation available to a spacecraft in deep space. The HI particle hit scrubbing algorithm (Equation 1) uses only a single backward difference to locate and correct particle hits, a procedure that was sufficient while the gyros were in use. However, attitude control gyros are known to wear out, and are generally one of the limiting factors for the nominal lifetime of a mission. Therefore any mission that has hopes of operating an extended mission must plan on having a gyroless attitude control option. Thus if stellar calibration and performance monitoring throughout an extended mission is required, it is essential that the stellar response should be robust to small pointing instabilities. The STEREO spacecraft were launched about a decade ago, and the hardware design, including the onboard computing capacity, was finalized at least 5 years before that. Since that time technology has advanced apace,

so a more sophisticated algorithm should be well within the onboard computational capacity of future missions. In particular a procedure using exposures both before and after the exposure being analyzed seems desirable.

Another desirable feature would be to eliminate the long gap between the last exposure of one image sequence and the first of the next, as the first exposures of the sequence dominate the false positives for particle hits. If gaps between images are unavoidable due to operational constraints, then the use of extra exposures solely for the particle detection algorithm may be a viable option.

7. SUMMARY

We have described a number of effects on the response of the STEREO-HI instruments to stellar signals that became apparent during careful analyses for the photometric calibration of the instruments.

We have shown that saturation is not a significant concern for the vast majority of stars. We have also found

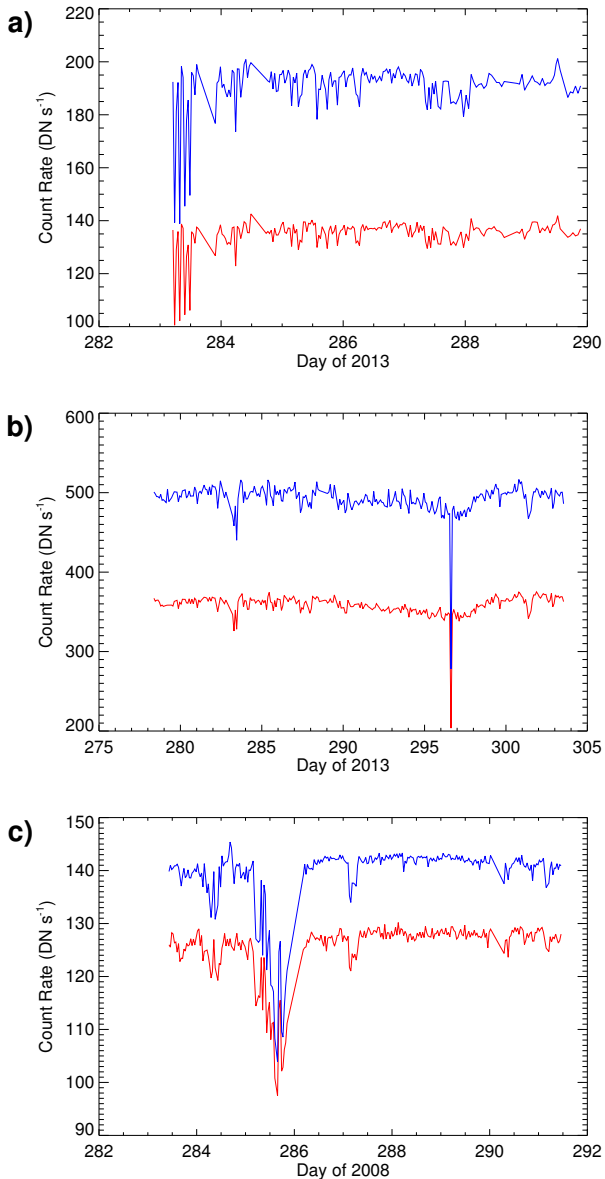


Figure 21. Comparison of the measured counting rates for selected pairs of moderately adjacent stars. a) HI-1A after the switch to gyroless attitude control. The stars are HD127 (red trace) and HD422 (blue) which are separated by 0.9° , the trace for HD127 has been multiplied by 2 to bring the traces closer together. b) HI-2A after the switch. The stars are HD17769 (red) and HD18700 (blue), which are separated by 4.7° . c) HI-1B near the momentum dump shown in Fig. 13. The stars are HD87176 (red), multiplied by 2, and HD87300 (blue), which are 0.24° apart. This interval covers the dip about 20 days after the momentum dump. Each plot covers the entire interval during which both stars were visible in that instrument.

that even for those stars that do have some saturation, it would still be possible to detect variations.

We have identified three ways in which the onboard cosmic ray scrubbing algorithm creates false positives from stellar signals:

1. When the STEREO spacecraft began gyroless operations. At this time the pointing stability (particularly in roll) was significantly degraded, though still within the mission requirements.
2. When HI-1B shifted relative to the spacecraft pointing, and in particular during the settling process after a major shift.
3. Due to the spacecraft orbital motion itself, this is particularly evident in the first exposure of a sequence.

We have shown that the particle hits spread parameter (Δ , Equation 5) can be used to flag times at which the effects of pointing fluctuations are severe. We have also shown that even at such times, the correlation between adjacent stars will allow corrections to be made.

We have found that the nominal AZP projection used by the HI astrometry routines is sufficiently accurate to allow reliable identification of stars.

We have also made some suggestions for improvements for future heliospheric imagers to reduce some of these problems. Such improvements would facilitate both calibration of the instruments, and also the astronomical exploitation of the data.

Astronomers wishing to use the HI data are urged to discuss their plans with the author for assistance in ensuring that the data are used as effectively as possible.

The *Heliospheric Imager* (HI) instruments were developed by a collaboration that included the Rutherford Appleton Laboratory and the University of Birmingham, both in the United Kingdom, and the Centre Spatial de Liège (CSL), Belgium, and the US Naval Research Laboratory (NRL), Washington DC, USA. The STEREO/SECCHI project is an international consortium of the Naval Research Laboratory (USA), Lockheed Martin Solar and Astrophysics Lab (USA), NASA Goddard Space Flight Center (USA), Rutherford Appleton Laboratory (UK), University of Birmingham (UK), Max-Planck-Institut für Sonnensystemforschung (Germany), Centre Spatial de Liège (Belgium), Institut d’Optique Théorique et Appliquée (France), and Institut d’Astrophysique Spatiale (France).

The author wishes to thank Dr C.J. Eyles, Dr J.A. Davies, Mr S.R. Crothers, Prof. R.A. Harrison, Prof. G.J. White

and Dr W.T. Thompson for valuable discussions and advice.

Software: SolarSoft (Freeland & Handy 1998) <http://www.lmsal.com/solarsoft/>

REFERENCES

- Belcheva M., Markov H., Tsvetanov Z., Iliev I., Stateva I. 2015, *BlgAJ*, 22, 28
- Bewsher D., Brown D.S., Eyles C.J., Kellet B.J., White G.J., Swinyard, B. 2010, *Solar Phys.* 264, 433.
- Brown D.S., Bewsher D., Eyles C.J. 2009, *Solar Phys.* 254, 185.
- Calabretta M.R., Greisen E.W. 2002, *A&A*, 395, 1077.
- Chaturvedi P., et al. 2014, *MNRAS*, 442, 3737
- Davis C.J., et al. 2012, *MNRAS*, 420, 1355.
- Driesman A., Hynes S., Cancro G. 2008, *Spa. Sci. Rev.* 136, 17.
- Eyles C.J., et al. 2003, *Solar Phys.* 217, 319.
- Eyles C.J., et al. 2009, *Solar Phys.* 254, 387.
- Freeland S. L., Handy B. N. 1998, *Solar Phys.* 182, 497.
- Holdsworth D. L., Rushton M. T., Bewsher D., Walter F. M., Eyres S. P. S., Hounsell R., Darnley M. J. 2014, *MNRAS*, 438, 3483
- Howard R. A., et al. 2008, *Spa. Sci. Rev.*, 136, 67 .
- Kaiser M.L., et al. 2008, *Spa. Sci. Rev.*, 136, 5.
- Myers J.R., Sande C.B., Miller A.C., Warren W.H., Jr., Tracewell D.A. 2001, *VizieR Online Data Catalog* 5109, <http://vizier.cfa.harvard.edu/viz-bin/VizieR?-source=V/109>.
- Paunzen E., Wraight K. T., Fossati L., Netopil M., White G. J., Bewsher D. 2013, *MNRAS*, 429, 119
- Sangaralingam V., Stevens I. R. 2011, *MNRAS*, 418, 1325
- Tappin S.J., Eyles C.J., Davies J.A. 2015, *Solar Phys.* 290, 2143.
- Tappin S.J., Eyles C.J., Davies J.A. 2017, *Solar Phys.* 292:28
- Valtonen M. J., Mikkola S., Lehto H. J., Gopakumar A., Hudec R., Polednikova J. 2011, *ApJ*, 742, 22
- Whittaker G. N., Stevens I. R., Sangaralingam V. 2013, *MNRAS*, 431, 3456
- Wraight K. T., White G. J., Bewsher D., Norton A. J. 2011, *MNRAS*, 416, 2477
- Wraight K. T., Bewsher D., White G. J., Nowotny W., Norton A. J., Paladini C. 2012, *MNRAS*, 426, 816
- Wraight K. T., Fossati L., Netopil M., Paunzen E., Rode-Paunzen M., Bewsher D., Norton A. J., White G. J. 2012, *MNRAS*, 420, 757
- Wraight K. T., Fossati L., White G. J., Norton A. J., Bewsher D. 2012, *MNRAS*, 427, 2298